KUOPION YLIOPISTON JULKAISUJA C. LUONNONTIETEET JA YMPÄRISTÖTIETEET 235
KUOPIO UNIVERSITY PUBLICATIONS C. NATURAL AND ENVIRONMENTAL SCIENCES 235

PETRO JULKUNEN

# Relationships between Structure, Composition and Function of Articular Cartilage

## Studies based on Fibril Reinforced Poroviscoelastic Modeling

Doctoral dissertation

To be presented by permission of the Faculty of Natural and Environmental Sciences
of the University of Kuopio for public examination in
Auditorium 1, Kuopio University Hospital,
on Friday 8th August 2008, at 12 noon

Department of Physics,
University of Kuopio
Department of Clinical Neurophysiology,
Kuopio University Hospital
Department of Clinical Physiology and Nuclear Medicine,
Kuopio University Hospital

KUOPION YLIOPISTO

KUOPIO 2008

Distributor: Kuopio University Library
P.O. Box 1627
FI-70211 KUOPIO
FINLAND
Tel. +358 17 163 430
Fax +358 17 163 410
http://www.uku.fi/kirjasto/julkaisutoiminta/julkmyyn.html

Series Editors: Professor Pertti Pasanen, Ph.D.
Department of Environmental Science

Professor Jari Kaipio, Ph.D.
Department of Physics

Author's address: Department of Clinical Neurophysiology
Kuopio University Hospital
P.O. Box 1777
FI-70211 KUOPIO
FINLAND
Tel. +358 44 717 4118
Fax +358 17 173 244
E-mail: petro.julkunen@kuh.fi

Supervisors: Professor Jukka S. Jurvelin, Ph.D.
Department of Physics
University of Kuopio

Rami K. Korhonen, Ph.D.
Department of Physics
University of Kuopio

Reviewers: Associate Professor Thomas M. Quinn, Ph.D.
Department of Chemical Engineering
McGill University, Montreal, QC
Canada

Assistant Professor Corrinus C. van Donkelaar, Ph.D.
Department of Biomedical Engineering
Eindhoven University of Technology, Eindhoven
The Netherlands

Opponent: Professor Robert L. Sah, M.D., Sc.D.
Department of Bioengineering
University of California, San Diego, CA
USA

ISBN 978-951-27-0973-1
ISBN 978-951-27-1088-1 (PDF)
ISSN 1235-0486

Kopijyvä
Kuopio 2008
Finland

Julkunen, Petro. Relationships between Structure, Composition and Function of Articular Cartilage - Studies based on Fibril Reinforced Poroviscoelastic Modeling.
Kuopio University Publications C. Natural and Environmental Sciences 235. 2008. 78 p.
ISBN 978-951-27-0973-1
ISBN 978-951-27-1088-1 (PDF)
ISSN 1235-0486

**ABSTRACT**

Articular cartilage is a highly specialized tissue at the ends of articulating bones. It provides a smooth and frictionless contact surface for joint movements. As cartilage degenerates in osteoarthrosis, joint motion causes pain and joint mobility decreases. During cartilage degeneration, the tissue exhibits changes in its mechanical properties even before the appearance of any visual symptoms. Since cartilage is composed of several components, i.e. collagen, proteoglycans (PGs) and interstitial water, the effect of these components on the mechanical response of cartilage and their role in the progression of osteoarthrosis needs to be carefully addressed.

In this thesis work, quantitative microscopy, magnetic resonance imaging (MRI) and finite element analysis were used to study the relation between tissue constituents and the mechanical behavior of cartilage. Specifically, the role of collagen architecture on cartilage mechanics was investigated. Furthermore, the mechanical behavior of articular cartilage was simulated using microscopically determined composition and structure of the tissue.

Collagen and PG contents of the tissue were found to be inter-related with the fibrillar (collagen specific) and non-fibrillar (PG specific) matrix moduli, respectively. Tissue permeability was associated with both collagen and PGs. The properties of the non-fibrillar cartilage matrix and intrinsic permeability were also found to correlate with the MRI longitudinal relaxation time, T1. Although the transverse relaxation time, T2, is known to reflect cartilage collagen architecture, determination of the collagen specific mechanical properties using MRI proved difficult. This was due to complexities in collagen architecture which were not reflected by the bulk T2. By accounting for the inhomogeneous collagen architecture in the model, the traditional indentation analysis of tissue modulus was improved. Finally, by applying the composition-based modeling theory, the mechanical behavior of human patellar cartilage under unconfined compression was predicted successfully using microscopically determined tissue composition and structure.

In conclusion, quantitative imaging techniques may provide tools for the assessment of cartilage mechanical integrity. However, due to the complex collagen architecture and its effect on the mechanical response of cartilage, the collagen-specific mechanical properties cannot be easily assessed with the current MRI techniques. The composition-based modeling, combined with the quantitative microscopy techniques of tissue composition and structure, may enable prediction of cartilage mechanical behavior without mechanical testing. In the future, the challenges of imaging collagen architecture with MRI need to be overcome to enable clinical functional imaging of articular cartilage.

National Library of Medicine Classification: QT 36, WE 103, WE 300, QU 55.3, QU 55.5
Medical Subject Headings: Cartilage, Articular; Biomechanics; Finite Element Analysis; Collagen; Proteoglycans; Permeability; Osteoarthritis; Materials Testing; Microscopy; Magnetic Resonance Imaging

To Hanna

**ACKNOWLEDGMENTS**

This study was carried out during the years 2004-2008 at the Department of Physics, University of Kuopio, as well as the Department of Clinical Neurophysiology and the Department of Clinical Physiology and Nuclear Medicine, Kuopio University Hospital. The study was made possible by many important people as well as grant-giving foundations.

I am deeply grateful to my principal supervisor Professor Jukka Jurvelin, Ph.D., for sharing his dedicated experience in the field, and for giving me the opportunity to work in such an interesting area of medical engineering as articular cartilage mechanics.

I sincerely thank my other supervisor Rami Korhonen, Ph.D., for getting me started in mechanical modeling of cartilage, for sharing his expertise on this topic, and always being thorough when it comes to research. I am also grateful for Rami for all the valuable personal discussion during these past years, and all the shared beers in the bars of Kuopio.

I am indebted to Wouter Wilson, Ph.D., University of Eindhoven, the Netherlands for his invaluable guidance during my thesis and his interest towards my work. Importantly, I thank him for his support as a friend.

I am grateful for the significant contribution of all the other co-authors, Professor Mikko Lammi, Ph.D., Professor Walter Herzog, Ph.D., Cheng-Juan Qu, Ph.D., Mikko Nissi, Ph.D., Panu Kiviranta, M.D. and Jarno Rieppo, M.D.

My cordial thanks go to the official pre-examiners of the thesis: Associate Professor Thomas Quinn, Ph.D. and Assistant Professor René van Donkelaar, Ph.D., for their expert opinion and views on ways to improve my thesis. I also acknowledge Ewen MacDonald, D.Pharm., for the linguistic review.

I have had the great privilege to work with several experts, who have motivated me during the time I was working on my thesis. I would like to thank the personnel of the Departments of Anatomy and Physics, University of Kuopio. Especially, I want to acknowledge all the other members of the Biophysics of Bone and Cartilage research group, for providing a convivial working atmosphere and involvement in guidance during the thesis studies: Professor Juha Töyräs, Ph.D., Docent Miika Nieminen, Ph.D., Mikko Hakulinen, Ph.D., Simo Saarakkala, Ph.D., Heikki Nieminen, Ph.D., Eveliina Lammentausta, Ph.D., Mikko Laasanen, Ph.D., Antti Aula, M.Sc. (Eng), Janne Karjalainen, M.Sc. (Eng), Ossi Riekkinen, M.Sc., Jatta Kurkijärvi, M.Sc., Erna Kaleva, M.Sc., Jani Hirvonen, M.Sc., Matti Timonen, B.Sc., Pauno Lötjönen and Tuomo Silvast.

I acknowledge CSC Finnish IT center for science for allowing me to use their computing equipment. Especially, I want to thank Reijo Lindgren, M.Sc., for providing valuable assistance in the finite element analyses at the beginning of the thesis project.

Furthermore, I am forever grateful to my wonderful parents Päivi and Kaarlo for always supporting me. Also, for the security and help they have provided throughout my entire life while investing in my education.

Also, I thank all my friends who have supported me and provided me with a secure social environment.

Most of all, I am deeply grateful to my loving girlfriend Hanna, for being very understanding and supporting, and for always being there for me.

For funding, I want acknowledge the North Savo Fund of Finnish Cultural Foundation, Foundation for Technology Advancement, Finland, Emil Aaltonen Foundation, Finland, Kuopio University Hospital and Biomaterial Graduate School, Finland.

Kuopio, 2008

Petro Julkunen

## NOMENCLATURE

| | |
|---|---|
| $a$ | radius of the indenter |
| $a_\lambda$ | wavelength-dependent absorptivity coefficient |
| $A$ | area |
| $A_{PG}$ | absorbance of PGs |
| $b$ | path length in absorptive material |
| $\boldsymbol{C}$ | stiffness tensor |
| $c^+, c^-$ | concentration of internal cations and anions, respectively |
| $c^*$ | salt concentration |
| $c_F$ | fixed charge density |
| $c_{F,0}$ | initial fixed charge density |
| $c_{F,eff}$ | effective fixed charge density |
| $c_{PG}$ | concentration of PGs |
| $E$ | Young's modulus in isotropic case |
| $e, e_0$ | current and initial void ratio |
| $E_0$ | initial collagen fibril modulus |
| $E_\epsilon$ | strain-dependent collagen fibril modulus |
| $\vec{e}_f, \vec{e}_{f,0}$ | current and initial fibril direction |
| $E_m$ | Young's modulus of the non-fibrillar matrix |
| $E_{mae}$ | mean absolute error |
| $E_{mse}$ | mean squared error |
| $F$ | reaction force |
| $G_m$ | shear modulus of the non-fibrillar matrix |
| $h$ | sample thickness |
| $\mathbf{I}$ | unit tensor |
| $I_0, I$ | initial and passed through light power |
| $J$ | volumetric deformation |
| $K$ | drag coefficient |
| $k_0, k$ | initial and strain-dependent permeability |
| $K_m$ | bulk modulus of the non-fibrillar matrix |
| $n$ | number of samples |
| $n^{exf}$ | extra-fibrillar fluid fraction |
| $n^f$ | fluid fraction |
| $n_s, n_{s,0}$ | current and initial solid fraction |
| $M$ | permeability coefficient |
| $p$ | statistical significance or fluid pressure |
| $r$ | Pearson correlation coefficient |
| $R$ | gas constant |

| | |
|---|---|
| $T$ | transmittance or absolute temperature |
| T1 | longitudinal relaxation time |
| T2 | transverse relaxation time |
| $T_c$ | chemical expansion stress |
| $Q$ | volume fluid flow |
| $\gamma^{\pm}_{int,ext}$ | internal or external activity coefficient |
| $\epsilon$ | strain or dilation |
| $\epsilon^s$ | axial or compressive strain |
| $\epsilon_f$ | fibril strain |
| $\eta$ | viscoelastic damping coefficient |
| $\Delta\pi$ | osmotic pressure |
| $\kappa$ | scaling factor used in the Hayes' solution |
| $\lambda$ | elongation of collagen fibril |
| $\mu$ | shear modulus |
| $\mu^f$ | electrochemical potential |
| $\nu_{eff}$ | effective Poisson's ratio |
| $\nu_m$ | Poisson's ratio of the non-fibrillar matrix |
| $\rho_S$ | mass density of the solid matrix |
| $\rho_z$ | relative collagen density |
| $\boldsymbol{\sigma}^E$ | effective solid stress tensor |
| $\sigma_f$ | fibril stress |
| $\boldsymbol{\sigma}_f$ | fibril stress tensor |
| $\boldsymbol{\sigma}_{rs}$ | real solid stress |
| $\boldsymbol{\sigma}_{rs,J}$ | real solid stress including the dependency of $J$ |
| $\boldsymbol{\sigma}^{s,f,t}$ | solid, fluid and total stress tensor |
| $\phi$ | diameter |
| $\phi^{s,f}$ | solid and fluid volume fractions |
| $\varphi_{ci}$ | osmotic pressure coefficient |
| $\omega_0$ | (absolute) indenter displacement |

## ABBREVIATIONS

| | |
|---|---|
| DD | digital densitometry |
| ECM | extracellular matrix |
| FCD | fixed charge density |
| FE | finite element |
| FMC | femoral medial condyle |
| FRPE | fibril-reinforced poroelastic |
| FRPVE | fibril-reinforced poroviscoelastic |
| FRPVES | fibril-reinforced poroviscoelastic swelling |
| FT-IRIS | Fourier transform infra-red imaging spectroscopy |
| GAG | glycosaminoglycan |
| HUM | humerus |
| IR | infrared |
| MRI | magnetic resonance imaging |
| OA | osteoarthrosis |
| PAT | patella |
| PG | proteoglycan |
| PLM | polarized light microscopy |
| TE | time-to-echo |
| TR | repetition time |
| TMP | tibial medial plateau |

## LIST OF ORIGINAL PUBLICATIONS

This thesis is based on the following original articles, which are referred to in the text by their Roman numerals:

**I** Uncertainties in indentation testing of articular cartilage: A fibril-reinforced poro-viscoelastic study
Julkunen, P., Korhonen, R. K., Herzog, W., Jurvelin, J. S.
*Medical Engineering & Physics*, **30**(4): 506-515, 2008.

**II** Characterization of articular cartilage by combining microscopic analysis with a fibril-reinforced finite-element model
Julkunen, P., Kiviranta, P., Wilson, W., Jurvelin, J. S., Korhonen, R. K.
*Journal of Biomechanics* **40**(8): 1862-1870, 2007.

**III** Mechanical characterization of articular cartilage by combining magnetic resonance imaging and finite-element analysis - a potential functional imaging technique
Julkunen, P., Nissi, M. J., Jurvelin, J. S., Korhonen, R. K.
*Physics in Medicine & Biology*, **53**(9): 2425-2438, 2008.

**IV** Stress-relaxation of human patellar articular cartilage in unconfined compression - Prediction of mechanical response by tissue composition and structure
Julkunen, P., Wilson, W., Jurvelin, J. S., Rieppo, J., Qu, C.-J., Lammi, M. J., Korhonen, R. K.
*Journal of Biomechanics*, **41**(9): 1978-1986, 2008.

# Contents

Chapter I

# Introduction

Articular cartilage is characterized by a three-dimensional collagen network, negatively charged proteoglycans (PGs), interstitial water and cells, i.e. chondrocytes [24, 120]. Several external and internal factors, e.g. abnormal or impact mechanical loading and/or joint inflammation, may lead to osteoarthrosis (OA). OA is characterized by a degradation of collagen and PGs, leading to impaired functional properties of the tissue [7, 119].

Structural changes occurring during maturation and degeneration of cartilage can be revealed by different imaging techniques, such as high resolution magnetic resonance imaging (MRI) or microscopy [2, 3, 9, 19, 131, 143, 186]. Modern microscopic methods enable detailed characterization of the microstructure and composition of articular cartilage [9, 19, 20, 71, 142, 146, 173, 174]. The spatial collagen architecture can be analyzed using polarized light microscopy (PLM) or MRI [70, 125, 127, 142, 197, 198, 200]. Fourier transform infrared imaging spectroscopy (FT-IRIS) can be used to analyze the spatial distribution of the fluid, PGs and collagen [18, 19, 20, 30, 134, 146, 148, 200]. PG distribution can also be quantified using digital densitometry (DD) [72, 130, 149, 180].

Degenerative changes of articular cartilage structure and composition sensitively affect the mechanical behavior of the tissue [8, 73, 75, 156]. Changes in the mechanical properties of the tissue occur even before the appearance of any visual symptoms [156]. However, optimal interpretation of the functional characteristics of the tissue necessitates the use of a valid theoretical model. Using a valid model, the mechanical characteristics of different tissue components, which have their own characteristic effects on cartilage mechanics, can be assessed [80]. Several theoretical models have been developed to characterize the mechanical behavior of articular cartilage [33, 34, 42, 43, 56, 80, 83, 93, 98, 102, 105, 106, 118, 167, 168, 171, 187, 188, 190, 191, 194]. Considering the fact that the inhomogeneous collagen architecture has a significant role in the mechanical behavior of articular cartilage [83], most of the models do not capture the effect of depth-dependent collagen architecture on the mechanical behavior of cartilage. The role of the inhomogeneous collagen architecture is especially significant in indentation geometry [83, 165], but also under unconfined compression [63].

The objective of this thesis work was to estimate the effects of structure and composition on cartilage function using several quantitative imaging techniques together with computational and experimental mechanical analyses. The ability to incorporate realistic tissue structure and composition from quantitative imaging techniques into a theoretical model may represent an important step towards understanding the role of biomechanics in the development, adaptation and degeneration of articular cartilage. Moreover, by taking into account the structural

inhomogeneity and depth-dependency, and changes in these parameters during OA, prediction of the mechanical changes occurring during the early stages of OA may become more realistic. The present thesis represents one step towards a more sensitive diagnostic tool to assess the onset of OA by characterizing the functional properties of articular cartilage with (non-invasive) imaging methods.

Chapter II

# Structure and function of articular cartilage

Articular cartilage is located in joints between articulating bones (fig. 2.1). It provides an almost frictionless surface for smooth joint movement, aided by the lubrication of the surrounding synovial fluid. In the knee, the meniscus lies between load bearing joint surfaces. The two menisci (fig. 2.1) absorb part of the loads that the joint experiences.

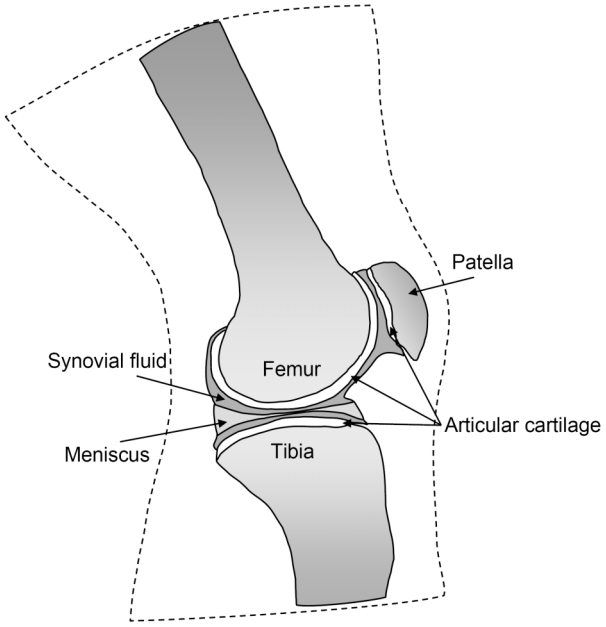


**Figure 2.1:** Schematic presentation of a knee joint. Frame of the knee is presented with dashed line. In this projection, only one of the two menisci is visible.

Articular cartilage can be described as a fibril-reinforced composite material consisting of a solid matrix and interstitial fluid (fig. 2.2). The main components in the solid matrix are two structural macromolecules, i.e. PGs and collagen. Cells (chondrocytes) are responsible for the synthesis of PGs and collagen [13, 28, 176]. The fluid phase contains water and solutes.

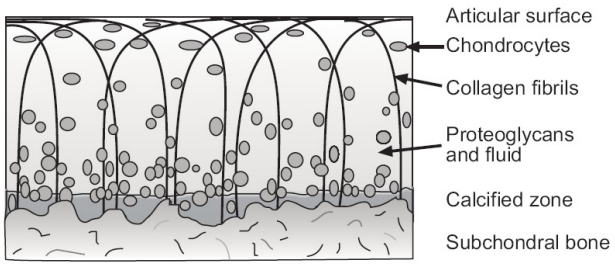


**Figure 2.2:** Schematic presentation of cartilage main constituents.

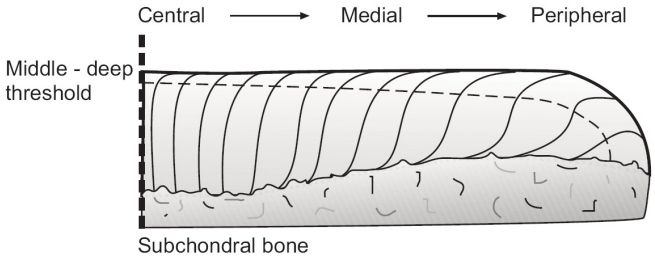


**Figure 2.3:** Schematic presentation of a normal collagen architecture. Additional laminae are visible depending on the location in the joint.

The interactions between collagen, PGs and fluid play an important role in the mechanical response of cartilage. During the development of OA, the mechanical properties of cartilage are weakened due to depletion of PGs and deterioration of collagen network. The degeneration of cartilage results in greater friction and eventually to pain and immobilization of a joint [26].

## 2.1 Structure and composition of articular cartilage

### 2.1.1 Collagen

Characteristically, 15-22% of the wet weight of articular cartilage is composed of collagen [119]. Several types of collagen have been identified in cartilage. About 90% is type II collagen, but also types I, III, V, VI, IX, X and XI have been found [9, 21, 36, 38, 201]. The collagenous network is stabilized by crosslinking of the collagen fibrils [37, 38, 193].

The primary collagen fibrils display a specific three-dimensional architecture (fig. 2.2), which has been suggested to be modulated by the loading of joints as well as by the maturation state of the tissue [67, 74, 124, 140, 144, 187]. The collagens are often oriented in distinct parallel planes, which appear as split-lines when cartilage is pricked with a pin [14, 17, 61, 116, 169]. Although the primary collagen fibrils are highly organized, randomly oriented secondary collagen fibrils have been observed with the scanning electron microscope [57, 66].

Normally, there are at least three zones (layers) in cartilage, which may be distinguished by the collagen orientation. In the superficial zone, the collagen fibrils are oriented parallel to

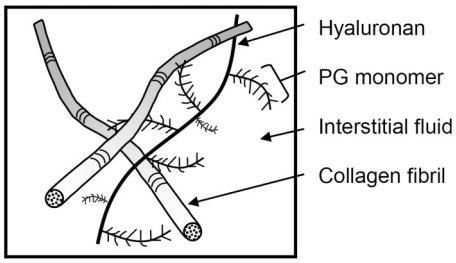


**Figure 2.4:** Schematic microstructure of articular cartilage tissue.

the cartilage surface. In the middle zone, the collagen fibrils bend towards a perpendicular-to-surface orientation. Below the middle zone is the deep zone, in which the fibrils are oriented perpendicular to the subchondral bone (fig. 2.2) [17]. Often a separate fourth zone, the calcified zone is recognized. In some species, several additional zones, laminae, may be distinguished [47, 74, 124, 127, 128, 140, 142, 196]. The laminar structure may also change depending on the location in a joint (fig. 2.3) [198].

A wide range of zonal thicknesses have been reported in the literature depending on species and the condition of the cartilage. Superficial, middle and deep zone thickness of 3-24%, 1-40% and 50-94% of the total cartilage thickness, respectively, have been reported [2, 3, 9, 31, 32, 52, 58, 149, 198].

### 2.1.2 Proteoglycans

PG monomers consist of a protein core and negatively charged glycosaminoglycans (GAGs) with carboxyl and sulphate groups resulting in a high fixed charge density (FCD) [110, 120] and leading to increased internal osmotic pressure and swelling of the tissue [49, 89, 172]. Monomers are further bound to a hyaluronan chain, which forms larger aggregates (fig. 2.4) [120, 121]. PGs are inhomogenously distributed in cartilage. In general, the PG content is the lowest in the superficial zone and increases towards the cartilage-subchondral bone interface [62, 139, 145, 146, 182]. PGs constitute 4-7% of cartilage wet weight [119].

### 2.1.3 Interstitial fluid

The predominant single component of cartilage is the interstitial fluid which accounts for 60-89% of the total cartilage wet weight, depending on the origin and integrity of cartilage [7, 75, 100, 119, 122, 132, 149, 150, 156, 157, 160, 161, 164, 177]. When cartilage is loaded by external forces, the porous structure of cartilage allows fluid to flow through the solid matrix. The water content is normally high in the superficial zone and it decreases with the cartilage depth [99, 129, 146, 163, 175].

## 2.2 Mechanical behavior of articular cartilage

The three-dimensional collagen architecture provides the dynamic and tensile strength for articular cartilage supported by the other tissue constituents. The collagen network affects the tensile strength due to the fibrillar structuring of collagens, which resists effectively tissue deformation in the direction of the fibrils [14]. The inhomogeneous structure of cartilage results in

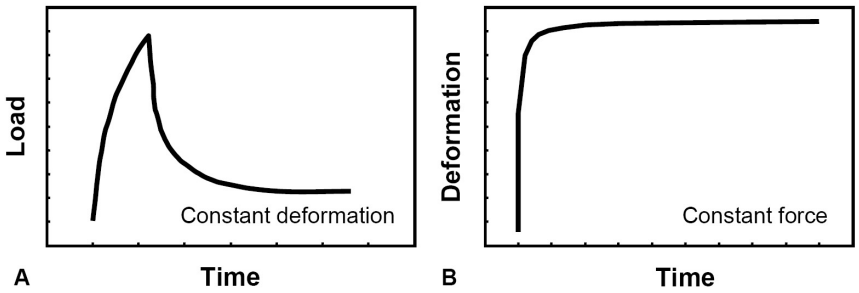


**Figure 2.5:** A) Stress-relaxation performed with slow strain-rate and B) creep compression.

a non-uniform fluid flow, inhomogeneous strains under loading, depth-dependent cell shape and depth-dependent tensile stiffness of cartilage [4, 63, 77, 79, 147]. The inhomogeneous structure is presumably caused by the remodeling of the collagen fibrils during maturation and loading [125, 144, 187]. The total fluid content in cartilage is controlled by the swelling pressures attributable to the fixed charges of PGs, as well as by the tensile stiffness of the collagen network that resists the swelling [112, 179]. PGs are considered to be mainly responsible for the static stiffness of cartilage [149]. A link between the fluid, PGs and collagen is established through the permeability of the cartilage matrix. The packing and orientation of collagen fibrils modulates the fluid flow in the tissue, and PGs resist the fluid flow throughout the tissue, both being factors which influence the permeability [40, 111, 113, 119, 136, 162].

Transient compressive mechanical behavior of cartilage can be determined by creep and stress-relaxation tests (fig. 2.5). In stress-relaxation, a deformation is applied on a sample and the induced force is measured. During the application of strain in stress-relaxation, the reaction forces are mainly modulated by the collagen network and fluid [80, 94, 95, 113]. During the strain application, the tissue resists fluid flow effectively through the low tissue permeability. Then the largest lateral deformation occurs, stressing the collagen fibrils in their tensile direction, exhibiting strain-dependent stiffening [98, 133]. In contrast, the equilibrium phase of the stress-relaxation is controlled mostly by the PGs [29, 35, 80, 149]. The relaxation phase mainly results from the cartilage matrix permeability, which is believed to be dependent on the PG and fluid content [111, 119, 136]. The permeability is also affected by the collagen fibrils [113].

In creep, a constant force is applied on a sample and the deformation is recorded. After the load application, the collagen fibril network together with fluid pressurization mainly prevents the deformation. Even though collagen does not have significant compressive stiffness due to its slender nature, it confines the tissue deformation in the tensile direction of the collagen fibrils, increasing the internal pressures of cartilage [64, 74, 165]. PGs begin to control the creep behavior when approaching equilibrium similarly as in stress-relaxation. The creep rate is mostly modulated by the tissue permeability [87, 97].

## 2.3 Osteoarthrosis

OA is a degenerative joint condition, which causes pain and reduces joint mobility [24, 27]. A reduced concentration of PGs, breakdown of collagen network as well as an increase in the water content and softening of the tissue have been associated with OA [10, 15, 24, 27,

108, 115]. Remodeling of subchondral bone, leading to stiffer and thicker subchondral bone, has also been associated with OA [76, 138, 184]. In early OA, the collagen degradation may lead to increased swelling and thickening of cartilage [11, 15]. The first visible signs of OA include fibrillation of cartilage surface, which extends to the deeper zones of cartilage during OA progression. As fibrillated fissures grow, the surface of cartilage is torn, releasing cartilage fragments into the surrounding joint space. At the same time, cartilage becomes thinner and there is enzymatic degradation in the tissue. Finally after cartilage fails to restore its normal structure, progressive loss of cartilage tissue leads to direct bone-to-bone contact [24, 27]. OA may occur spontaneously, or it may result from a trauma or change in the loading environment, e.g. after meniscus damage [39, 55, 152, 164].

Adult articular cartilage has been shown to have a limited ability to repair the structural changes which typically occur in OA [25]. These changes are sensitively detectable via the alterations in the mechanical properties of cartilage [7, 15, 75, 87, 123, 150, 156]. Therefore, techniques which permit the characterization of cartilage mechanics are essential if one wishes to prevent or detect OA. A combination of imaging techniques and mechanical modeling might represent one option to accomplish this goal.

CHAPTER III

# Fibril-reinforced modeling of articular cartilage

Articular cartilage is characterized as an inhomogeneous, anisotropic and poroviscoelastic tissue [26, 105]. However, these natural characteristics were not taken into account in the first cartilage models. In the 1970's Hayes et al. introduced an isotropic elastic solution to model indentation of articular cartilage [53]. Since then the cartilage models have evolved from homogeneous biphasic or poroelastic isotropic or transversely isotropic [118], conewise linear elastic [167], fibril-reinforced [80, 98] through triphasic [60, 89] and poroviscoelastic [34, 171] to inhomogeneous poroelastic [93] or poroviscoelastic fibril-reinforced [191] with swelling [190] and composition-based fibril-reinforced models [188, 189]. The development of cartilage models is presented in more detail in the following sections. The emphasis will be placed on the fibril-reinforced models, which were examined in this thesis work.

## 3.1 Biphasic background

Biphasic and/or poroelastic mixture theories are the basis for most of the articular cartilage models [1, 7, 50, 80, 93, 98, 118, 166, 167, 188, 191]. These models separate the fluid from the solid phase.

In a biphasic model, the fluid flow within the cartilage matrix is included. The solid and fluid phases are intrinsically non-dissipative and incompressible, and the flow of fluid in and out is the only dissipative factor. The total stress in a biphasic material is:

$$\boldsymbol{\sigma}^t = \boldsymbol{\sigma}^s + \boldsymbol{\sigma}^f = -p\mathbf{I} + \boldsymbol{\sigma}^E, \tag{3.1}$$

where $\boldsymbol{\sigma}^s$, $\boldsymbol{\sigma}^f$ and $\boldsymbol{\sigma}^t$ are the solid, fluid and total stress tensors, respectively, $p$ is the fluid pressure, $\mathbf{I}$ is the unit tensor and $\boldsymbol{\sigma}^E$ is the effective solid stress tensor. At equilibrium, the effective solid stress tensor is the only component resisting the deformation when the fluid flow has ceased [118], and the fluid pressure controls the dynamic and transient behavior of cartilage. The dominating mechanism responsible for the creep and stress-relaxation behavior in a biphasic model is the diffusive drag coefficient ($K$), which defines the relative motion between the solid and fluid phases:

$$K = \frac{(n^f)^2}{k}, \tag{3.2}$$

where $n^f$ is the fluid volume fraction and $k$ is the permeability. One generally widely recognized theory to describe fluid flow through a porous material is Darcy's law, which states that the

fluid flow $Q$ through an area $A$ is proportional to the permeability of the medium $k$ and the ratio between the fluid pressure difference $\Delta p$ and the penetration depth $h$:

$$Q = Ak\frac{\Delta p}{h}. \tag{3.3}$$

The permeability of the tissue is highly dependent on the tissue dilation ($\epsilon$) [91]:

$$k = k_0 \mathrm{e}^{M\epsilon}, \tag{3.4}$$

where $k_0$ is the initial permeability and $M$ is constant. This theory was further developed by van der Voet for implementation in FE models to consider the local void ratios in the tissue [181]:

$$k = k_0\left(\frac{1+e}{1+e_0}\right)^M, \tag{3.5}$$

where $e_0$ and $e$ are the initial and current void ratio, respectively. The void ratio is defined as the ratio between the fluid ($n^f$) and solid ($n_s$) volume fraction:

$$e = \frac{n^f}{n_s} = \frac{1-n_s}{n_s}. \tag{3.6}$$

## 3.2 Fibril-reinforced models

In the fibril-reinforced models of cartilage, the tissue is assumed to be biphasic (see Chapter 3.1), and the solid matrix is divided into a fibrillar and non-fibrillar part [44, 77, 79, 80, 83, 93, 94, 95, 96, 97, 98, 137, 188, 190, 191]. The fibrillar part mimics collagen fibrils, while the non-fibrillar part describes mainly PGs (fig. 3.1). A swelling effect due to negative charges in cartilage are also included in some fibril-reinforced model [48, 79, 89, 137, 188, 189, 190, 195].

### 3.2.1 Non-fibrillar part

**Hookean model**

A Hookean model describes the behavior of a linear elastic solid material. It has been applied commonly for modeling the non-fibrillar matrix of articular cartilage [74, 80, 92, 93, 98, 122, 191]. For the linearly elastic non-fibrillar matrix, the effective solid stress ($\boldsymbol{\sigma}_{nf}$) is described using the stiffness matrix $\boldsymbol{C}$ and the total elastic strain tensor $\boldsymbol{\epsilon}$:

$$\boldsymbol{\sigma}_{nf} = \boldsymbol{C}\boldsymbol{\epsilon}. \tag{3.7}$$

**Neo-Hookean model**

Instead of the traditional Hookean model, the stress of the non-fibrillar matrix can be described using, for instance, a neo-Hookean model [190]:

$$\boldsymbol{\sigma}_{nf} = K_m\frac{\ln(J)}{J}\mathbf{I} + \frac{G_m}{J}(\mathbf{F}\cdot\mathbf{F}^{\mathbf{T}} - J^{2/3}\mathbf{I}), \tag{3.8}$$

where $K_m$ is the bulk modulus, $G_m$ is the shear modulus and $\mathbf{F}$ is the deformation gradient tensor. The neo-Hookean model has a non-linear stress-strain behavior and, in contrast to the Hookean model, it is applicable for large deformations [190].

The stress of the non-fibrillar part of the solid matrix in a composition-based model [188] can be described with the same neo-Hookean description (eq. 3.8). Even though the non-fibrillar material itself is assumed to be incompressible, the solid matrix is compressible due to

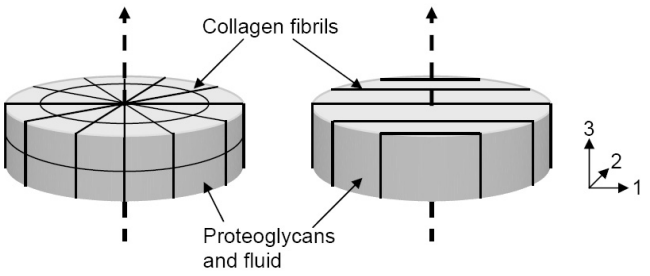


**Figure 3.1:** Schematic presentation of a continuum fibril field in an axisymmetric (left) and three-dimensional model, including split-lines (right).

its porous structure. Based on this assumption, the composition dependent Poisson's ratio can be described as:

$$\nu_m = 0.5 n_s = 0.5 \frac{n_{s,0}}{J}, \tag{3.9}$$

where $n_s$ and $n_{s,0}$ are the current and initial solid volume fractions, respectively. Due to previous assumptions, $\nu_m$ approaches the value of 0.5 as the solid fraction approaches the value of 1. Similarly, $\nu_m$ approaches 0, as the solid volume fraction disappears completely.

### 3.2.2 Fibrillar part

**Elastic and viscoelastic fibril description**

For the fibrillar matrix of the fibril-reinforced poroelastic (FRPE) model, Li et al. introduced a linear strain-dependency of the collagen fibril network modulus ($E_f$) with tensile strain ($\epsilon_f$) [98]:

$$E_f = E_0 + E_\epsilon \epsilon_f, \tag{3.10}$$

where $E_0$ represents the initial fibril network modulus and $E_\epsilon$ the strain-dependent fibril network modulus (fig. 3.2A). The fibril stress of a viscoelastic collagen fibril in the fibril-reinforced poroviscoelastic (FRPVE) model can be described by the following equation [191]:

$$\sigma_f = \begin{cases} -\frac{\eta}{2\sqrt{(\sigma_f - E_0\epsilon_f)E_\epsilon}}\dot{\sigma_f} + E_0\epsilon_f + \left(\eta + \frac{\eta E_0}{2\sqrt{(\sigma_f - E_0\epsilon_f)E_\epsilon)}}\right)\dot{\epsilon_f} & \epsilon_f > 0 \\ 0 & \epsilon_f \leq 0 \end{cases} \tag{3.11}$$

where $\eta$ is the viscoelastic damping coefficient, $E_0$ and $E_\epsilon$ are the initial and strain-dependent fibril moduli, respectively, $\epsilon_f$ is the fibril strain, and $\dot{\sigma_f}$ and $\dot{\epsilon_f}$ are the stress- and strain-rate, respectively.

Recently, Wilson et al. introduced a novel viscoelastic fibril model, which is based on the same schematic model as that previously presented (fig. 3.2B). However, the strain-dependency was described in a different way [188]. The stresses of spring S1 and S2 are exponentially strain-dependent [153]:

$$P_1 = E_1(e^{k_1\epsilon_f} - 1) \tag{3.12}$$

and

$$P_2 = E_2(e^{k_2\epsilon_f} - 1), \tag{3.13}$$

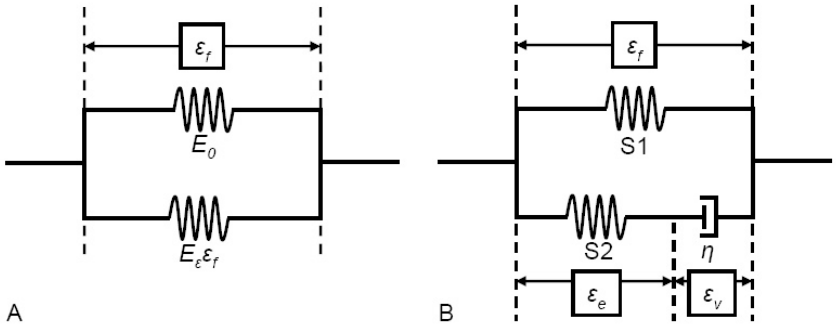


**Figure 3.2:** Presentation of a non-linear elastic (A) and non-linear viscoelastic (B) collagen fibril.

where $P_1$ and $P_2$ are the stresses of springs S1 and S2 in tension, respectively, and $E_1$, $E_2$, $k_1$ and $k_2$ are material constants. The strain of the spring S2 is also dependent on the strain of the viscous dashpot. The dashpot has the same stress as the spring S2:

$$P_2 = \eta\dot{\epsilon}_v = \eta(\dot{\epsilon}_f - \dot{\epsilon}_e). \tag{3.14}$$

Wilson et al. presented a time-dependent solution for $P_2$ [188]:

$$P_2 = -\frac{b}{2} + \frac{1}{2}\sqrt{b^2 - 4c}, \tag{3.15}$$

with

$$b = \frac{\epsilon_f^{t+\Delta t} - \epsilon_f^t}{\Delta t}\eta + \frac{\eta}{k_2\Delta t} + E_2 \tag{3.16}$$

$$c = \frac{\epsilon_f^{t+\Delta t} - \epsilon_f^t}{\Delta t}\eta E_2 - \frac{\eta P_2^t}{k_2\Delta t}. \tag{3.17}$$

Combining the stress components $P_1$ and $P_2$ for the collagen fibrils, the first Piola-Kirchhoff fibril stress becomes:

$$P_f = P_1 + P_2. \tag{3.18}$$

**Primary and secondary fibrils**

In some fibril-reinforced models of cartilage, the collagen fibrils align parallel to the cartilage surface throughout the tissue depth [80, 93, 98]. Li et al. introduced an inhomogeneous model of cartilage with depth-dependent material properties [93], but the orientation of the fibrils was still lacking. In a fibril-reinforced model with realistic collagen orientation, the fibrillar part can be divided into primary and secondary collagen fibrils. The initial fibril directions of the primary fibrils can be implemented into a model according to realistic collagen orientations, while the secondary fibrils have an isotropic structure through the tissue depth (fig. 3.3) [191].

At an integration point, for each (4 primary and 13 secondary) fibril ($i$), the initial orientation is given by a fibril direction vector ($\vec{e}_{f,0}$). Using the deformation tensor ($\mathbf{F}$), the logarithmic fibril strain for each fibril can be computed:

$$\epsilon_f = \log\|\mathbf{F}\cdot\vec{e}_{f,0}\|. \tag{3.19}$$

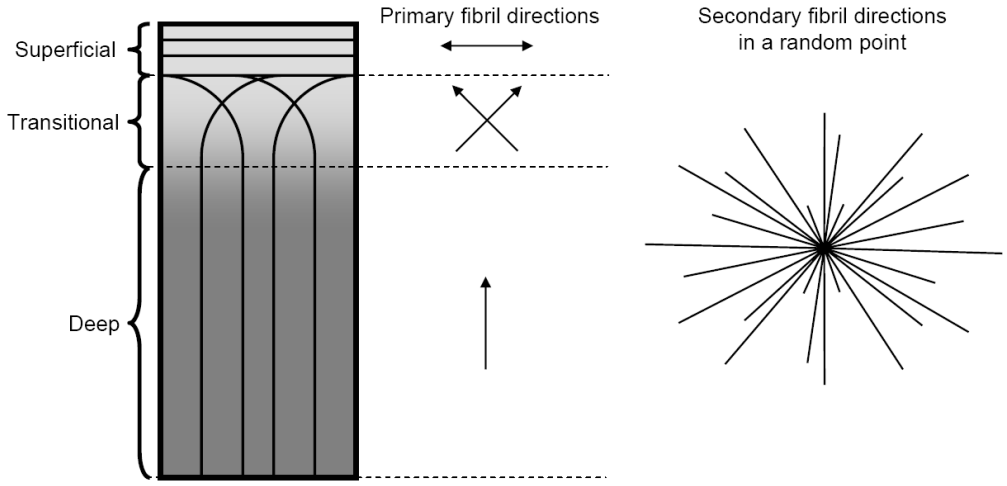


**Figure 3.3:** Schematic presentation of the collagen architecture in some fibril-reinforced models [79, 188, 190, 191]. In the superficial zone, the collagen fibrils are aligned parallel to the cartilage surface, bending in the middle/transitional zone to achieve the perpendicular-to-surface orientation in the deep zone. Examples of primary fibrils implemented in each cartilage zone of the model are presented next to the schematic presentation. Secondary fibrils represent the less organized collagen network at any given point of the tissue. The secondary fibril directions are similar at each integration point.

After deformation, the reorientation of each fibril is simulated by computing the current fibril direction ($\vec{e}_f$):

$$\vec{e}_f = \frac{\mathbf{F} \cdot \vec{e}_{f,0}}{\|\mathbf{F} \cdot \vec{e}_{f,0}\|}. \tag{3.20}$$

Then, the tensile fibril stress tensor ($\boldsymbol{\sigma}_f$) can be derived from the tensile stresses of the individual fibrils in the direction of the fibrils ($\sigma_f$) [189]:

$$\boldsymbol{\sigma}_f = \sigma_f \vec{e}_f \vec{e}_f. \tag{3.21}$$

For Piola-Kirchhoff fibril stress (eq. 3.18), the fibril stress (Cauchy stress) can be solved:

$$\boldsymbol{\sigma}_f = \frac{\lambda}{J} P_f \vec{e}_f \vec{e}_f, \tag{3.22}$$

where $\lambda$ is the elongation of the fibril [188].

Stresses for the primary and secondary collagen fibrils are defined as [188, 191]:

$$\sigma_{f,p} = \rho_{c,p} \sigma_f^{t+\Delta t} \tag{3.23}$$

$$\sigma_{f,s} = \rho_{c,s} \sigma_f^{t+\Delta t}, \tag{3.24}$$

where the relative fibril densities for the primary and secondary fibrils ($\rho_{c,p}$, $\rho_{c,s}$) [190] are:

$$\rho_{c,p} = \rho_{c,tot} \frac{C}{4C + 13} \tag{3.25}$$

$$\rho_{c,s} = \rho_{c,tot}\frac{1}{4C+13}, \tag{3.26}$$

with a positive constant $C$ and the depth-dependent total collagen fraction per total solid volume $\rho_{c,tot}$. Total fibril stress is defined as a sum of the individual fibril stresses ($\boldsymbol{\sigma}_f^i$), as:

$$\boldsymbol{\sigma}_f = \sum_{i=1}^{totf} \boldsymbol{\sigma}_f^i, \tag{3.27}$$

where $i$ is the index of a single fibril and $totf$ is the total number of fibrils in an integration point.

### 3.2.3 Swelling

**Osmotic swelling**

Due to the higher concentration of charges in articular cartilage than in the surrounding fluid, the excess ions cause a pressure gradient called the Donnan swelling pressure gradient ($\Delta\pi$), which is described as:

$$\Delta\pi = \pi_{int} - \pi_{ext} = RT[\phi_{int}(c^+ + c^-) - 2\phi_{ext}c_{ext}], \tag{3.28}$$

where $\pi_{int}$ and $\pi_{ext}$ are the internal and external osmotic pressures, which are dependent on the concentrations of the internal cations ($c^+$) and anions ($c^-$), external salt concentration ($c_{ext}$), internal ($\phi_{int}$) and external ($\phi_{ext}$) osmotic coefficients, the gas constant $R$ (8.314 J/(K mol)) and absolute temperature $T$ (310K) [59, 60]. Ion concentrations can be calculated as [59, 188]:

$$c^{\pm} = \frac{\pm c_F + \sqrt{c_F^2 + 4\frac{(\gamma_{ext}^{\pm})^2}{(\gamma_{int}^{\pm})^2}c_{ext}^2}}{2}, \tag{3.29}$$

where $\gamma_{int}^{\pm}$ and $\gamma_{ext}^{\pm}$ are the internal and external activity coefficients and $c_F$ is the FCD. Combining equations 3.28 and 3.29, the osmotic pressure becomes:

$$\Delta\pi = \phi_{int}RT\left(\sqrt{c_F^2 + 4\frac{(\gamma_{ext}^{\pm})^2}{(\gamma_{int}^{\pm})^2}c_{ext}^2}\right) - 2\phi_{ext}RTc_{ext}. \tag{3.30}$$

The FCD can be expressed as a function of the volumetric tissue deformation tensor $J$ [188]:

$$c_F = c_{F,0}\left(\frac{n^{f,0}}{n^{f,0} - 1 + J}\right), \tag{3.31}$$

where $c_{F,0}$ and $n^{f,0}$ are the initial FCD and fluid fraction, respectively. The fluid fraction can also be divided into intra- and extrafibrillar fluid fractions. As part of the fluid is entrapped within the collagen fibrils, its ability to interact with the charged tissue particles becomes reduced [114]. When the FCD is scaled with the extra-fibrillar water volume fraction ($n^{exf}$), the effective FCD can be considered as:

$$c_{F,eff} = \frac{n^f c_F}{n^{exf}}. \tag{3.32}$$

The extra-fibrillar water volume fraction may be defined as:

$$n^{exf} = \frac{\rho_s n^{exf,m}}{1 - n^{exf,m} + \rho_s n^{exf,m}}, \tag{3.33}$$

where $\rho_s$ is the mass density of the solid matrix, and the extra-fibrillar water mass fraction is:

$$n^{exf,m} = n^{f,m} - n^{inf,m} = n^{f,m} - \varphi_{ci}\rho_{c,tot,m}, \tag{3.34}$$

where $n^{f,m}$ and $n^{inf,m}$ are the mass fraction of the total and intra-fibrillar water, respectively. $\varphi_{ci}$ is the mass of intra-fibrillar water per collagen mass and $\rho_{c,tot,m}$ is the collagen mass fraction with respect to the total wet weight, defined as:

$$\rho_{c,tot,m} = (1 - n^{f,m}) \sum_{i=1}^{totf} \rho_c^i. \tag{3.35}$$

The dependence of $\varphi_{ci}$ from the osmotic pressure gradient (eq. 3.30) can be described by [114, 188]:

$$\varphi_{ci} = 0.448e^{-0.328\Delta\pi} + 0.822. \tag{3.36}$$

**Chemical expansion**

Chemical expansion results from repulsion between large negative groups in the solid matrix. The chemical expansion stress ($T_c$) was defined by Lai et al. [89] as:

$$T_c = a_0 c_F \left( - \kappa \frac{\gamma_{ext}^{\pm}}{\gamma_{int}^{\pm}} \sqrt{c^-(c^- + c_F)} \right), \tag{3.37}$$

with material constants $a_0$ and $\kappa$.

### 3.2.4 Total stress

Previously presented theories can be combined into different models depending on the application. The models are presented here in the order of their appearance in the literature (table 3.1), and two of them were applied in the present thesis; a fibril-reinforced poroviscoelastic model (FRPVE) [191] in studies I-III, and a fibril-reinforced composition-based model [188] in study IV.

**Fibril-reinforced poroviscoelastic model (FRPVE)**

For the FRPVE model, a linear elastic non-fibrillar matrix is implemented (eq. 3.7). The fibrillar part is implemented based on viscoelastic fibril stress (eq. 3.27) with an inhomogeneous collagen architecture (fig. 3.3). Then, the total stress (eq. 3.1) for the FRPVE model can be solved as [191]:

$$\boldsymbol{\sigma}^t = \boldsymbol{\sigma}_{nf} + \sum_{i=1}^{totf} \boldsymbol{\sigma}_f^i - p\mathbf{I}. \tag{3.38}$$

**Fibril-reinforced poroviscoelastic swelling model (FRPVES)**

The FRPVES model combines viscoelastic fibrils (eq. 3.11) with an inhomogeneous collagen architecture (fig. 3.3), neo-Hookean non-fibrillar matrix (eq. 3.8), osmotic swelling (eq. 3.30) and chemical expansion (eq. 3.37) [190]. Thus, the total tissue stress becomes:

$$\boldsymbol{\sigma}^t = \boldsymbol{\sigma}_{nf} + \sum_{i=1}^{totf} \boldsymbol{\sigma}_f^i - \Delta\pi\mathbf{I} - \mu^f\mathbf{I} - T_c\mathbf{I}, \tag{3.39}$$

where $\mu^f$ is the electrochemical potential of water [89].

**Fibril-reinforced composition-based model**

The fibril-reinforced composition-based model can predict the mechanical behavior of a material by its composition and structure [188]. Hence, the mechanical moduli are no longer used to describe material behavior such as was the case in the former models. The composition-based model combines the viscoelastic collagen fibril description (eq. 3.22), neo-Hookean non-fibrillar matrix (eq. 3.8), osmotic swelling (eq. 3.30) and chemical expansion (eq. 3.37). The total stress can be depicted by:

$$\boldsymbol{\sigma}^t = \frac{n_{s,0}}{J}\boldsymbol{\sigma}_{rs} - \Delta\pi\mathbf{I} - \mu^f\mathbf{I} - T_c\mathbf{I} = n_{s,0}\boldsymbol{\sigma}_{rs,J} - \Delta\pi\mathbf{I} - \mu^f\mathbf{I} - T_c\mathbf{I}, \tag{3.40}$$

where $n_{s,0}$ is the initial solid volume fraction, $J$ is the volumetric deformation and $\boldsymbol{\sigma}_{rs,J}$ is the real solid stress including the dependency of $J$. Wilson et al. excluded chemical expansion in the original model [188]. By applying the rule of mixture, the total solid stress is defined as:

$$\boldsymbol{\sigma}_{rs,J} = (1 - \sum_{i=1}^{totf}\rho_c^i)\boldsymbol{\sigma}_{nf} + \sum_{i=1}^{totf}\rho_c^i\boldsymbol{\sigma}_f^i, \tag{3.41}$$

where $\rho_c^i$ is the volume fraction of the collagen fibrils with respect to the total solid volume in the fibril $i$. When the previous equation is combined with eq. 3.40, the total stress becomes:

$$\boldsymbol{\sigma}^t = n_{s,0}((1 - \sum_{i=1}^{totf}\rho_c^i)\boldsymbol{\sigma}_{nf} + \sum_{i=1}^{totf}\rho_c^i\boldsymbol{\sigma}_f^i) - \Delta\pi\mathbf{I} - \mu^f\mathbf{I} - T_c\mathbf{I}. \tag{3.42}$$

**Table 3.1:** Development of stress tensors in fibril-reinforced models of articular cartilage.

| Material model | Citation | Total stress |
|---|---|---|
| Fibril-reinforced poroviscoelastic (FRPVE) | [191] | $\boldsymbol{\sigma}^t = \boldsymbol{\sigma}_{nf} + \sum_{i=1}^{totf} \boldsymbol{\sigma}_f^i - p\mathbf{I}$ |
| Fibril-reinforced poroviscoelastic swelling (FRPVES) | [190] | $\boldsymbol{\sigma}^t = \boldsymbol{\sigma}_{nf} + \sum_{i=1}^{totf} \boldsymbol{\sigma}_f^i - \Delta\pi\mathbf{I} - \mu^f\mathbf{I} - T_c\mathbf{I}$ |
| Fibril-reinforced composition-based* | [188] | $\boldsymbol{\sigma}^t = n_s((1 - \sum_{i=1}^{totf} \rho_c^i)\boldsymbol{\sigma}_{nf} + \sum_{i=1}^{totf} \rho_c^i \boldsymbol{\sigma}_f^i)$ $-\Delta\pi\mathbf{I} - \mu^f\mathbf{I} - T_c\mathbf{I}$ |

*Chemical expansion was not included in the present thesis with the fibril-reinforced composition-based model.

**Symbols:**

| | |
|---|---|
| $\boldsymbol{\sigma}^t$ | total stress |
| $\boldsymbol{\sigma}_{nf}$ | stress of non-fibrillar matrix |
| $totf$ | number of fibrils |
| $\boldsymbol{\sigma}_f^i$ | stress of $i$th fibril |
| $\mu^f$ | chemical potential of water |
| $\Delta\pi$ | osmotic pressure gradient |
| $T_c$ | chemical expansion stress |
| $\mathbf{I}$ | unit tensor |
| $n_s$ | solid volume fraction |
| $\rho_c^i$ | collagen solid fraction of $i$th fibril |

CHAPTER IV

# Aims, hypothesis and significance

The present work aims at providing novel information about the structure - function relationships in articular cartilage, with a special goal to increase our understanding of the roles of cartilage components in the mechanical characteristics of the tissue. Moreover, this work represents an advance towards obtaining functional imaging of articular cartilage. The general hypothesis is to prove that structure/content determines the mechanical behavior of the tissue, and that knowing the content and structure is therefore essential if one wishes to estimate the tissue mechanics. This is important because deteriorations in the mechanical properties cause problems in OA. Previous studies have shown that the composition and structure of cartilage can be quantified by chemical and microscopic analysis or MR-imaging. However, the mechanical role of cartilage constituents (collagen, PGs and fluid) has not been thoroughly investigated. Furthermore, the composition has not been successfully used to describe the mechanical behavior of cartilage. The specific aims of the thesis were to;

- estimate the error sources in clinically applicable mechanical indentation of articular cartilage and to improve the accuracy of present indentation analysis,
- relate mechanical properties of articular cartilage determined using the FE method to quantified microscopically determined compositional parameters,
- relate mechanical properties of articular cartilage determined using the FE method to MRI-derived parameters of articular cartilage,
- predict the mechanical response of articular cartilage under unconfined compression by using microscopically and biochemically obtained information on imaged tissue composition and structure only.

Related to the specific aims, the following hypotheses were examined;

- indentation response would be highly modulated by the structure of cartilage as well as the loading conditions. Thus, inclusion of the inhomogeneous Benninghoff-type architecture for the collagen network should enable a more accurate assessment of cartilage properties during indentation,
- collagen content would be correlated with the modulus of the collagen fibrils and PG content would be correlated with the modulus of the non-fibrillar matrix,
- changes in the mechanical properties of articular cartilage constituents (collagen and PGs) would be reflected in the altered MRI parameters,

- composition-based model, as constructed using microscopically determined composition and structure, would be able to simulate the compressive transient behavior of articular cartilage.

The information gained in this thesis will relate the composition and structure with the mechanical behavior of cartilage. The thesis will provide important insights into the challenges to be met by *in vivo* imaging and mechanical testing techniques. This thesis represents an important step towards functional imaging of cartilage by providing a link between tissue structure and function.

Chapter V

# Materials and methods

This thesis work utilizes several methods and techniques to assess the role of tissue composition and structure on cartilage mechanics. These methods include mechanical testing, Fourier transform infrared imaging spectroscopy (FT-IRIS), polarized light microscopy (PLM), digital densitometry (DD), magnetic resonance imaging (MRI), biochemical analysis and FE modeling.

The composition of cartilage samples was assessed by using FT-IRIS (for collagen and PGs), DD (for PGs), MRI or biochemical analyses. The structure of the collagen network was examined using PLM or MRI. The mechanical properties and responses of cartilage were assessed using compressive mechanical tests under indentation and unconfined compression. FE modeling was used to examine the mechanical properties of the cartilage constituents, e.g. collagen, PGs and fluid, and their effects on tissue responses. This thesis consists of four (I-IV) studies for which the materials and methods have been summarized in table 5.1. Some of the experimental tests were performed originally for other studies, as indicated in the table. All the methods have been described in detail below.

## 5.1 Samples and study protocols

Bovine articular cartilage samples were examined experimentally (mechanical testing) and numerically in studies I, II and III. Human cartilage samples were investigated in studies III and IV. In studies II, III and IV, microscopical or MRI techniques were used to obtain information of the cartilage structure and composition. In study IV, biochemical analyses were utilized together with quantitative microscopy to determine cartilage composition and structure.

**Study I**: Osteochondral bovine samples ($n = 26$, $r = 6.5$ mm, $h = 1.4 \pm 0.3$ mm) were harvested by drilling and freeing them from patella ($n = 8$), femur ($n = 9$) and humerus ($n = 9$) [81]. Two indentation experiments were performed for the samples using indenters with different diameters. Subsequently, full-thickness cartilage plugs were dissected from the osteochondral plugs, which were then tested in unconfined compression geometry. Poisson's ratios for the samples were optically measured under 10 % axial strain [65]. Based on the FRPVE simulations, the effects of tissue structure and loading rate on mechanical response were tested.

**Study II**: Cylindrical, full thickness articular cartilage samples ($n = 22$, $r = 1.9 \pm 0.1$ mm, $h = 1.4 \pm 0.3$ mm) from bovine patellar ($n = 7$), humeral ($n = 7$), femoral ($n = 4$) and tibial ($n = 4$) sites were harvested using a biopsy punch ($\phi = 3.7$ mm) and a razor blade. The samples were then mechanically tested in unconfined compression and analysed using PLM, FT-IRIS and DD

**Table 5.1:** Summary of the samples and methods applied. Experimental testing and imaging of studies I-III were originally performed for other studies, which are cited.

| Study | Material | $n$ | Loading geometry | Site | FE model | Other methods |
|---|---|---|---|---|---|---|
| **I** | Bovine [81] | 26 | Unconfined compression<br>Indentation | FMC<br>PAT<br>HUM | FRPVE | - |
| **II** | Bovine [74, 81] | 22 | Unconfined compression | FMC<br>HUM<br>PAT<br>TMP | FRPVE | PLM<br>FT-IRIS<br>DD |
| **III** | Bovine<br>Human [127] | 10<br>11 | Unconfined compression | PAT | FRPVE | MRI<br>PLM |
| **IV** | Human | 5 | Unconfined compression | PAT | Composition-based | PLM<br>FT-IRIS<br>Biochemistry<br>Histological grading |

**Abbreviations:**

| | |
|---|---|
| DD | digital densitometry |
| FMC | femoral medial condyle |
| FRPVE | fibril-reinforced poroviscoelastic |
| FT-IRIS | Fourier transform infrared imaging spectroscopy |
| HUM | humerus |
| MRI | magnetic resonance imaging |
| PAT | patella |
| PLM | polarized light microscopy |
| TMP | tibial medial condyle |

[74]. Poisson's ratios for the samples were also optically measured under 10 % axial strain [65]. Composition information from DD and FT-IRIS were then compared with the FRPVE model parameters obtained with these samples.

**Study III**: Cylindrical, full thickness articular cartilage samples ($n = 21$, $r = 2.0 \pm 0.1$ mm, $h = 2.3 \pm 0.7$ mm) from bovine and human patella were prepared [127]. For the use of human samples in the experiments, approval from National Authority of Medicolegal Affairs was obtained (no. 1781/32/200/01). All the samples were tested in unconfined compression, imaged using MRI and then characterized using numerical techniques. The collagen network architectures of the samples were also analyzed using MRI, and for comparison using PLM. MRI parameters were then compared with the FRPVE model parameters of these samples.

**Study IV**: Samples ($n = 5$, $r = 2.0 \pm 0.0$ mm, $h = 2.5 \pm 0.5$ mm) of cadaver knee joints were removed from the patellar surfaces with the approval from the National Authority for Medicolegal Affairs, Helsinki, Finland (no. 1781/32/200/01). Osteochondral pieces (16 mm in diameter) were drilled to be used in the analyses. Two adjacent full-thickness articular cartilage samples were removed from each osteochondral sample; one for microscopy and biochemical analyses, and one for mechanical testing using a razor blade and a biopsy punch of 4mm in diameter. All the samples were tested under unconfined compression and composition-based

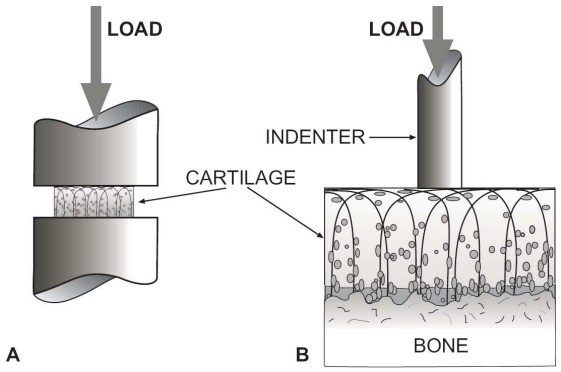


**Figure 5.1:** A) Unconfined compression and B) indentation geometry.

modeling was used to predict the tissue mechanics from the cartilage composition.

## 5.2 Mechanical testing

Compressive mechanical testing of articular cartilage is traditionally performed using one of three loading geometries: unconfined compression, confined compression or indentation. Unconfined compression and confined compression are applicable only *in vitro*, whereas indentation may also be applied clinically *in vivo* during arthroscopy [6, 87, 103, 104, 155, 156].

In this thesis work, a custom-made high resolution material testing device was used for mechanical tests [74, 80, 81, 122, 178]. The samples were first equilibrated under an offset stress or strain. Thereafter unconfined compression (studies I-IV, fig. 5.1A) or indentation (study I, fig. 5.1B) was performed up to 10-20% surface-to-surface strain in a single or several stress-relaxation steps. Subsequently, the Poisson's ratio (radial to axial strain ratio) was optically determined under 10% surface-to-surface strain in studies I and II [65].

### 5.2.1 Unconfined compression

**Study I, II**: In unconfined compression, a pre-stress of 12.5 kPa was applied to ensure full contact between the cartilage sample and the metallic plates. Then, a compression was applied up to a total of 20% surface-to-surface strain in four stress-relaxation steps. A compression rate of 1 $\mu$m/s was used during each step and a relaxation criterion of $< 100$ Pa/min was applied before starting the next stress-relaxation step. The reaction forces and deformations were recorded through the experiments. In addition, Poisson's ratios were recorded optically under 10% strain [65]. In study I, the equilibrium Young's moduli of the samples were determined from the recorded force and deformation curves.

In study II, the measured effective Poisson's ratios ($\nu_{eff}$) were implemented in the models by using an approximation of the non-fibrillar matrix Poisson's ratio ($\nu_m$). This approximation was based on two assumptions:

- A value of 0.5 (incompressible matrix) for $\nu_{eff}$: $\nu_m$ was also set to 0.5 due to the negligible resistance of the collagen network towards lateral deformation [64, 74],

- A value of 0.1 for $\nu_{eff}$: a $\nu_m$ value of 0.15 was used based on the publication by Wilson et al. [191].

From these assumptions, a linear dependency between the effective and non-fibrillar matrix Poisson's ratio was determined as follows:

$$\nu_m = 0.875\nu_{eff} + 0.0625. \tag{5.1}$$

**Study III, IV**: Stress-relaxation tests in unconfined compression were performed up to a 10% surface-to-surface strain in two stress-relaxation steps, after first applying a 5 % pre-strain. A compression rate of 1 $\mu$m/s was used during each compression step and a relaxation criterion of $<$ 39 Pa/min was applied before starting the next step. The reaction forces and axial deformations were recorded throughout the experiments.

### 5.2.2 Indentation

**Study I**: Indentation testing of all the samples was performed using plane-ended, permeable indenters ($\phi$ = 1.0 and 3.0 mm) [83]. Indentation stress-relaxation steps were performed up to a 20% surface-to-surface strain in four steps. Compression rate of 1 $\mu$m/s and $<$ 100 Pa/min relaxation criterion were used. The reaction forces and deformations were recorded through the experiments. Indentation moduli were derived for the samples using the isotropic elastic solution for the indentation problem proposed by Hayes et al. [53]. Indentation problem arises from mathematical difficulties in modeling elastic properities of the tissue via indentation tests due to tissue boundary confinement at the cartilage-bone interface and cartilage tissue surrounding the indented tissue part. For this purpose, a sample-specific scaling factor, dependent on the indenter radius $a$, cartilage thickness $h$ and effective Poisson's ratio of the tissue ($\nu_{eff}$) was used [53]. The indentation shear modulus ($\mu$) can be calculated as:

$$\mu = \frac{(1-\nu_{eff})\pi a}{4\kappa h}\frac{\sigma^s}{\epsilon^s}, \tag{5.2}$$

where $\sigma^s$ and $\epsilon^s$ are the isotropic stress and strain, respectively, and $\kappa$ is a scaling factor (eq. 5.5). The previous equation is only applicable for the plane-ended indenters. Shear modulus is related to Young's modulus ($E$) through Poisson's ratio:

$$E = 2\mu(1+\nu_{eff}). \tag{5.3}$$

For the isotropic indentation, the Young's modulus can be solved from eq. 5.2 with the aid of eq. 5.3 as:

$$E = \frac{F(1-\nu_{eff}^2)}{2\kappa a\omega_0}, \tag{5.4}$$

where $\omega_0$ is the absolute deformation of the tissue and $F$ is the measured force. The scaling factor $\kappa$ can then be derived from eq. 5.4 as:

$$\kappa = \frac{F(1-\nu_{eff}^2)}{2aEh\epsilon}. \tag{5.5}$$

Values for $\kappa$ as introduced for plane-ended indentation by Hayes et al. [53] are listed in table 5.2.

**Table 5.2:** Scaling factors as introduced by Hayes et al. [53].

| | **effective Poisson's ratio ($\nu_{eff}$)** | | | | | | | | | | | |
|---|---|---|---|---|---|---|---|---|---|---|---|---|
| $a/h$ | 0.05 | 0.10 | 0.15 | 0.20 | 0.25 | 0.30 | 0.35 | 0.40 | 0.42 | 0.44 | 0.46 | 0.48 |
| 0.2 | 1.180 | 1.183 | 1.187 | 1.192 | 1.198 | 1.207 | 1.218 | 1.232 | 1.240 | 1.248 | 1.257 | 1.268 |
| 0.4 | 1.406 | 1.413 | 1.422 | 1.434 | 1.451 | 1.472 | 1.502 | 1.542 | 1.562 | 1.586 | 1.613 | 1.645 |
| 0.6 | 1.665 | 1.677 | 1.693 | 1.715 | 1.744 | 1.784 | 1.839 | 1.917 | 1.957 | 2.004 | 2.061 | 2.129 |
| 0.8 | 1.946 | 1.963 | 1.986 | 2.018 | 2.063 | 2.124 | 2.211 | 2.338 | 2.405 | 2.486 | 2.583 | 2.704 |
| 1.0 | 2.239 | 2.260 | 2.291 | 2.334 | 2.395 | 2.480 | 2.603 | 2.789 | 2.890 | 3.013 | 3.166 | 3.359 |
| 1.2 | 2.538 | 2.564 | 2.602 | 2.656 | 2.734 | 2.845 | 3.008 | 3.261 | 3.402 | 3.576 | 3.795 | 4.085 |
| 1.4 | 2.842 | 2.872 | 2.917 | 2.982 | 3.076 | 3.214 | 3.421 | 3.748 | 3.934 | 4.169 | 4.473 | 4.878 |
| 1.6 | 3.147 | 3.181 | 3.233 | 3.309 | 3.421 | 3.586 | 3.839 | 4.247 | 4.484 | 4.788 | 5.189 | 5.737 |
| 1.8 | 3.455 | 3.492 | 3.550 | 3.637 | 3.767 | 3.960 | 4.261 | 4.756 | 5.048 | 5.429 | 5.941 | 6.659 |
| 2.0 | 3.763 | 3.804 | 3.868 | 3.966 | 4.113 | 4.336 | 4.685 | 5.272 | 5.624 | 6.089 | 6.726 | 7.644 |

## 5.3 Finite element analyses

FE simulations were used to determine the mechanical properties for articular cartilage samples (studies II and III), to estimate the effect of varying structure/composition on the mechanical behavior of cartilage (studies I-IV), and to validate modeling of the mechanical behavior of cartilage through the composition-based theory (study IV). In all the studies, unconfined compression or indentation tests were simulated. The models were implemented and solved using ABAQUS 6.4 (Abaqus Inc., Providence, RI, USA).

### 5.3.1 Geometries, meshes and material properties

**Studies I-IV**: The loading was applied in unconfined compression geometry. The geometry was based on the true sample size measured with a stereomicroscope (Nikon SMZ-10, Nikon Inc., Japan). Axisymmetric meshes consisting of 288 4-node pore pressure continuum elements (fig. 5.2A) were used. The FRPVE model (studies I-III) or the composition-based model (study IV) were used to define the material properties of the cartilage samples.

**Study I**: In addition to unconfined compression, indentation geometry was applied. For the indentation simulations, the meshes were constructed to achieve aspect-ratios (indenter radius-to-sample thickness ratio) from 0.2 to 2. This was separately done for two impermeable plane ended indenters ($\phi$ = 1 and 3 mm). Each indentation mesh consisted of 480 axisymmetric 4-node pore pressure continuum elements (fig. 5.2B). The criteria on the sample size set by Spilker et al. were satisfied [170]. During the unconfined compression simulations, samples of 3.7 mm in diameter were created and the thickness was varied to correspond to the thickness values used in the indentation. The FRPVE model was used.

### 5.3.2 Boundary conditions

**Studies I-IV**: For axisymmetric unconfined compression simulations, the boundary conditions were set as follows:

- zero pore pressure at the cartilage edge to indicate free fluid flow,
- axial movement of the nodes at the cartilage bottom was restricted,
- lateral movement at the axis of symmetry was restricted,

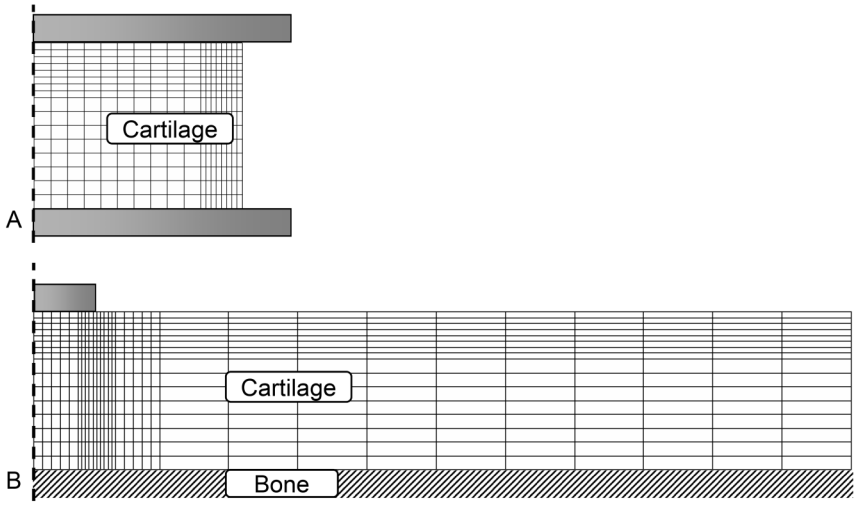


**Figure 5.2:** Axisymmetric finite element meshes used in A) unconfined compression (studies I-IV) and B) indentation (study I) .

- in stress-relaxation, a deformation condition was set on the cartilage surface nodes to simulate tissue compression.

**Study I**: For axisymmetric indentation simulations, the following boundary conditions were assumed:

- zero pore pressure at the cartilage edge and surface (when not in contact with the indenter),
- axial and lateral movements of the nodes at the cartilage-bone interface were restricted,
- lateral movement at the axis of symmetry was restricted,
- deformation boundary condition was set for the indenter to simulate the compression.

**Study IV**: During the free-swelling step, the boundary conditions were set as follows:

- zero pore pressure at the cartilage edge and top,
- axial movement of the nodes at the cartilage bottom was restricted,
- lateral movement at the axis of symmetry was restricted.

### 5.3.3 Simulations

**Study I**: Unconfined compression and indentation tests were simulated for cartilage samples with a Benninghoff-type collagen architecture and varying thickness and Poisson's ratios. Cartilage thickness was varied systematically to simulate different aspect-ratios (0.2 - 2). The material properties (fibril network stiffness) for the simulated cartilage samples were varied to achieve the effective Poisson's ratios of 0.05 to 0.42. The effective Poisson's ratios were determined from unconfined compression simulations. From the simulations with the FRPVE model

with unchanged Benninfhoff-type structure, novel scaling factors were computed from eq. 5.5 for the calculation of equilibrium and dynamic indentation modulus. These scaling factors take into account the inhomogeneous collagen architecture. In the equation, $F$ was the reaction force obtained from indentation simulations, and $E$ and $\nu_{eff}$ were the Young's modulus and Poisson's ratio obtained from unconfined compression simulations.

Separately, the effect of compression rates from 0.1 $\mu$m/s to 4 mm/s on the reaction forces and consequently on the scaling factors was simulated for the aspect ratios of 0.2, 1, 1.5 and 2. Finally, the effect of the collagen architecture on the detected equilibrium and peak forces was simulated using various combinations of the superficial and middle zone thickness.

**Study II**: Unconfined compression was simulated in two stress-relaxation steps using the experimental loading protocol. Each sample-specific FE model was fitted to the corresponding stress-relaxation curve by minimizing the mean absolute error ($E_{mae}$) between the experimental and simulated reaction force curves:

$$E_{mae} = \frac{1}{n}\sum_{j=1}^{n}\left|\frac{F_{model,j} - F_{exp,j}}{F_{exp,j}}\right|, \tag{5.6}$$

where $F_{model,j}$ and $F_{exp,j}$ are the simulated and experimental reaction force values at any time-point ($j$). The optimized model parameters were $E_0$, $E_\epsilon$, $E_m$, $M$ and $k_0$. The viscoelastic damping coefficient $\eta$ was fixed to 947 MPa/s [191, 192]. The curve fitting was achieved using the multi-dimensional nonlinear minimization routine available in Matlab (MathWorks inc., Natick, MA, USA).

**Study III**: Unconfined compression was simulated in two stress-relaxation steps using the experimental loading protocol. Each sample-specific FE model was fitted to the corresponding stress-relaxation curve by minimizing the mean squared error ($E_{mse}$) between the experimental and simulated force curves:

$$E_{mse} = \frac{1}{n}\sum_{j=1}^{n}\left(\frac{F_{model,j} - F_{exp,j}}{F_{exp,j}}\right)^2. \tag{5.7}$$

The optimized model parameters were $E_0$, $E_\epsilon$, $E_m$, $M$ and $k_0$. The viscoelastic damping coefficient $\eta$ was fixed to 947 MPa/s [191, 192].

**Study IV**: Unconfined compression was simulated with a loading protocol corresponding to that of the experimental loading protocol. A realistic structure and composition of cartilage was implemented in three FE models, which were then fitted simultaneously to the corresponding stress-relaxation curves by minimizing the mean squared error (eq. 5.7) between the experimental and simulated force curves. The optimized parameters were $E_1$, $E_2$, $k_1$, $k_2$, $k_0$, $n_0$. Using the optimized model parameters, the stress-relaxation responses of the two remaining samples were predicted solely based on the cartilage composition and structure.

## 5.4 Microscopy

Microscopical techniques are able to characterize collagen, PGs and water spatially in articular cartilage. PLM was used in studies II-IV, FT-IRIS in studies II and IV, and DD in study II.

- PLM can be used to measure the depth-dependent collagen orientation [141, 142].
- FT-IRIS can be used to evaluate the collagen, PG and water distribution in cartilage [30, 134, 146].
- DD can be applied to quantify the PG distribution, when Safranin O staining is used [72, 130].

### 5.4.1 Polarized light microscopy

PLM can be used to analyze the collagen network architecture of articular cartilage [74, 127, 141, 142]. Before imaging, the samples (studies II-IV) were fixed in formalin, decalcified, dehydrated, embedded in paraffin, and cut into five-$\mu$m-sections and the PGs were removed [9, 70, 142].

In a polarized light microscope, two linear polarizers are positioned perpendicular to each other preventing light to pass through them without a specimen in between them. When an optically anisotropic cartilage sample, due to the collagen fibrils, is positioned between the polarizers, the state of polarization is altered causing light to pass through the second linear polarizer. Then birefringence can be determined from grayscale images according to the inverse-Fresnell equation [9]. Also other parameters such as collagen orientation can be estimated from PLM [142].

The measurement system consisted of a Leitz Ortholux BK-II pol (Leitz Wetzlar, Wetzlar, Germany) polarized light microscope equipped with precision grade polarization optics and monochromatic light source. Peltier-cooled 12-bit CCD-camera (Photometrics SenSys, Photometrics Inc., Tucson, AZ, USA) was used to acquire the images.

### 5.4.2 Fourier transform infrared imaging spectroscopy

FT-IRIS is widely used in the material sciences to help in the characterization of chemical composition of specimens. The FT-IR technique is based on the measurement of wavelength dependent IR absorption (fig. 5.3A). IR energy is either reflected or transmitted through the sample and part of the energy is absorbed. IR radiation has sufficient energy to cause vibrations of the molecules. The vibration frequency, the wavelengths at which the molecule absorbs energy are molecule-specific. Most functional groups absorb above 1500 $cm^{-1}$. The region below 1500 $cm^{-1}$ is known as the "fingerprint region". Every molecule has a unique absorption pattern in the fingerprint region, which can be used for the characterization of material composition (i.e. collagen and PG). Several thousands of spectra can be measured which means that this is a powerful instrument allowing the detection of chemical composition and in that way it can help to depict the tissue characteristics (fig. 5.3B).

Before imaging, the samples (studies II and IV) were embedded into an OCT compound, frozen, cut into 10 $\mu$m-thick sections and transferred to a barium fluoride window for measurement [30, 142]. The imaging instrument used in the FT-IRIS analyses was PerkinElmer Spectrum 300 (PerkinElmer, Inc., Shelton, CT, USA). The used spectral resolution was 8 $cm^{-1}$. For the quantification of collagen content in cartilage, the Amide I peak (1710-1610 $cm^{-1}$) was used, and for the spatial assessment of the PG content, the carbon region (1075-975 $cm^{-1}$) was used [30, 78, 134, 146].

In the analysis of the depth-dependent collagen distribution, Amide I (collagen specific [30, 146, 142]) absorption was converted to depth-wise collagen mass-fraction by using the bulk collagen solid mass fraction obtained from the biochemical analyses, i.e. the average value of the depth-wise Amide I absorbance profile was first scaled to match the biochemically measured bulk collagen solid mass fraction and the depth-dependent mass fraction was then calculated.

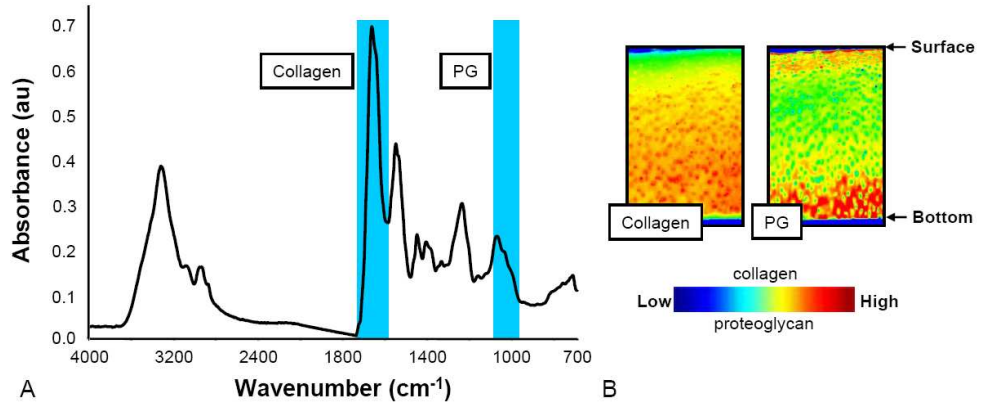


**Figure 5.3:** A) IR absorption distribution spectrum from a single human cartilage sample. B) Spatial collagen and PG content distributions for a human articular cartilage sample.

The depth-wise PG distribution was determined similarly from the biochemically determined PG content and the depth-dependent FT-IRIS data of carbon region [19, 20, 30, 134, 146]. Volume fractions of the collagen and PG distributions were estimated through the assumed solid tissue density ($\rho_S$= 1.4338 g/ml [16, 163, 189]).

Using the biochemical analysis of collagen and PG contents and the FT-IRIS analyses of the solid (collagen + PGs) content distributions, the water mass fraction profile was estimated as a complement of the solid fraction [146]. The total water volume fraction was derived from the water mass fraction through the assumed solid mass density ($\rho_S$=1.4338 g/ml) using eq. 3.33 [16, 163, 189].

### 5.4.3 Digital densitometry

PG content in articular cartilage can be quantified optically using the color reactions between PGs and a specific dye. The dye molecules should bind stoichiometrically with PGs. The optical density (OD) measurement is based on the Beer-Lambert law, which states that the absorbance (OD) of a substance is directly proportional to the concentration of that substance. The general Beer-Lambert law for PG absorbance is:

$$A_{PG} = a_\lambda b c_{PG}, \tag{5.8}$$

where $a_\lambda$ is the wavelength-dependent absorptivity coefficient, $b$ is the path length, and $c_{PG}$ is the PG concentration. Experimental measurements are made in terms of transmittance ($T$), which is defined as:

$$T = \frac{I}{I_0}, \tag{5.9}$$

where $I$ is the power of light after it passes through the sample and $I_0$ is the initial light power. The relation between $A_{PG}$ and $T$ is:

$$A_{PG} = -\log_{10}(T) = -\log_{10}\frac{I}{I_0}. \tag{5.10}$$

The above-mentioned theory was utilized to measure the PG concentration of Safranin O stained histological sections using DD [72, 74, 130]. In this part of the study (study II), the samples were fixed in formalin, decalcified, dehydrated and embedded in paraffin. The samples were then cut to five-$\mu$m-thick sections and stained using Safranin O [130]. Measurements were conducted with the Leitz Orthoplan (Leitz Wetzlar, Wetzlar, Germany) microscope and images were captured with the Peltier-cooled 12-bit CCD-camera (Photometrics CH 250, Photometrics Inc., Tucson, AZ, USA).

## 5.5 Magnetic resonance imaging

MRI can probe the magnetic characteristics of cartilage water that interact with the macromolecular constituents, i.e. collagen and PGs. MRI techniques were used in study III to determine spatial sample-specific T1 and T2 relaxation times from which the collagen architectures of cartilage samples were estimated.

### 5.5.1 MRI Relaxation times

**T1 and T2 relaxation time**: For the analysis of T1 and T2 relaxation times, the samples were imaged at 25 °C using a 9.4 T vertical magnet (Oxford Instruments Plc., Witney, UK) with the following single spin echo sequence parameters for T2: TR = 2500, TE = 14, 24, 34, 44, 64, 84 ms. Following the T2 analysis, T1 relaxation times were analysed using a saturation recovery spin echo sequence (TE = 14, TR = 200, 500, 1000, 1500, 3000, 5000 ms). Slice thickness of 1 mm and 10 mm field-of-view with a matrix size of 256 x 64 induced a depth-wise resolution of 39 $\mu$m. The MRI parameter maps were fitted to a mono-exponential two-parameter function, and depth-wise relaxation time profiles were calculated by averaging 3-pixel-wide columns along the articular surface [126]. Bulk values of T1 and T2 were calculated for each sample.

**T2 structural analysis**: Arranged tissue structures, such as collagen in articular cartilage, organize and restrict the motion of the surrounding water. While the dipolar interactions between water protons are averaged out in isotropic tissues, the magnetic fields of arranged protons interact with nearby protons depending on their arrangement with respect to each other and the magnetic field. As a result, an orientation dependent T2 relaxation rate that is governed by the term $(3\cos q^2 - 1)$ is minimized when the "magic angle" of $q = 54.7^o$ is reached [154].

When the articular surface of a specimen is arranged perpendicular to the static magnetic field, the anisotropic arrangement of fibrils leads to varying dipolar interactions with tissue depth. This results in an anisotropic T2 relaxation time of the tissue that follows the collagen fibril orientation [2, 46, 85, 125, 127, 197, 198, 199].

In order to implement a realistic collagen architecture into the FE model, three cartilage zones were determined from T2 profiles. The first and second boundaries were determined as the half-maximum locations of the rising and descending parts, respectively, of the bell-shaped T2 curve, according to a method adapted from Xia et al. (fig. 5.4) [199]. However, as the bovine cartilage often had more than three structural laminae [74, 125, 127], the complex collagen architectures (5 and 7 laminae) were incorporated into the FE models by using the same principle.

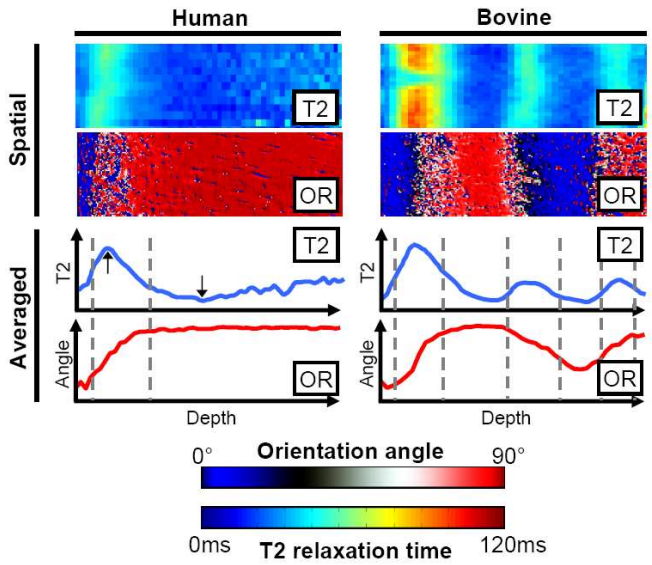


**Figure 5.4:** Dependence of the depth-wise T2 relaxation time on the orientation angle (OR), as determined using polarized light microscopy. For the estimation of orientation angles from T2, the method introduced by Xia et al. was applied [199]. All the laminar boundaries are presented for human and bovine (with its multilaminar structure) samples with dashed vertical lines. In the figures, the cartilage surface is on the left. From the spatial T2 and OR maps, parallel-to-surface slices were used for resolving averaged OR and T2 curves.

## 5.6 Biochemical analyses

The samples reserved for biochemical analyses (study IV) were analyzed for their water, PG and collagen mass fraction as well as FCD. The wet weight of the samples was measured after their immersion in phosphate buffered saline. Then, the samples were freeze-dried, and the dry weight of the tissue was determined. From the wet and dry tissue weight, the bulk fluid fraction was derived [135, 177].

The solid collagen mass fraction of the samples was estimated from the spectrophotometric assay for hydroxyproline after hydrolysis of the freeze-dried tissue samples [23, 158, 177]. Each sample was analyzed as three replicates. The yield of hydroxyproline in hydrolysis was estimated using hydrolyzed collagen type I from rat tail, based on the nominal hydroxyproline content of collagen. This information was then used to correct the total collagen content of the samples. Finally, the hydroxyproline content was normalized against the wet and dry weights of each sample.

For the PG content analysis, the samples were digested for 24 h at 60 °C with 1 mg ml$^{-}$1 of papain (Sigma, Germany) in 5 mM cysteine and 5 mM EDTA in 150 mM sodium phosphate buffer. The PG contents of the papain-digested samples were estimated by quantifying their total uronic acid content in a spectrophotometric assay [22, 135].

Total fixed charge density (FCD) was estimated from the molar ratios of uronic and sialic

acid, as well as glucosamine and galactosamine of extracted bovine cartilage PGs. Depth-wise FCD, as well as collagen and PG contents, was then determined using the FT-IRIS-derived collagen and PG distributions (see Chapter 5.4.2).

## 5.7 Histological grading

In order to reveal differences in the degenerative stages of the samples in study IV, they were graded using a histological grading method, i.e. the Mankin score [107]. Histological sections, subjected to Safranin-O staining, were "blind-coded" and investigated under the microscope by three individual researchers. The sample-specific Mankin scores were calculated as a mean of the three scores.

## 5.8 Statistical analyses

**Study I**: Wilcoxon signed ranks test was used to compare differences between the indentation moduli, determined with Hayes' and novel scaling factors, and unconfined compression moduli.

**Study II**: Kruskall-Wallis Post Hoc test was used to estimate the site-dependent differences in the assessed cartilage properties. Pearson correlation coefficients ($r$) were determined to indicate relationships between the cartilage composition (collagen and PGs) and mechanical parameters.

**Study III**: Linear Pearson correlation coefficients were determined for the relationships between the MRI- and mechanical parameters.

**Study IV**: Linear Pearson correlation coefficients were determined between the experimental and simulated reaction forces.

# Chapter VI
# Results

## 6.1 Uncertainties in indentation analysis

Differences were observed between the scaling factors presented by Hayes et al. [53] and those presented in study I (Study I: fig. 7). Similarly, significant ($p < 0.001$) differences were found between the isotropic equilibrium Young's moduli estimated after the indentation tests by using the Hayes' solution and the value obtained from the FRPVE model (Study I: table 1). In addition, minor differences between the novel scaling factors determined for indenters of 1mm and 3mm in diameter were noted (tables 6.1 and 6.2). The above mentioned differences were also detected for the dynamic moduli and scaling factors.

**Table 6.1:** Novel scaling factors for the 1mm diameter indenter that was introduced in study I (see table 5.2).

| | **effective Poisson's ratio ($\nu_{eff}$)** | | | | | | | | | | | |
|---|---|---|---|---|---|---|---|---|---|---|---|---|
| $a/h$ | 0.05 | 0.10 | 0.15 | 0.20 | 0.25 | 0.30 | 0.35 | 0.40 | 0.42 | 0.44 | 0.46 | 0.48 |
| 0.2 | 1.600 | 1.579 | 1.551 | 1.516 | 1.474 | 1.424 | 1.367 | 1.303 | 1.275 | 1.246 | 1.216 | 1.185 |
| 0.4 | 1.697 | 1.690 | 1.681 | 1.671 | 1.658 | 1.643 | 1.626 | 1.608 | 1.600 | 1.591 | 1.583 | 1.574 |
| 0.6 | 1.901 | 1.916 | 1.931 | 1.945 | 1.960 | 1.974 | 1.988 | 2.002 | 2.008 | 2.013 | 2.019 | 2.024 |
| 0.8 | 2.150 | 2.186 | 2.225 | 2.267 | 2.312 | 2.359 | 2.409 | 2.462 | 2.484 | 2.507 | 2.530 | 2.553 |
| 1.0 | 2.418 | 2.480 | 2.548 | 2.621 | 2.699 | 2.783 | 2.872 | 2.966 | 3.005 | 3.045 | 3.086 | 3.128 |
| 1.2 | 2.710 | 2.798 | 2.895 | 3.000 | 3.113 | 3.234 | 3.364 | 3.502 | 3.559 | 3.618 | 3.679 | 3.740 |
| 1.4 | 3.012 | 3.124 | 3.248 | 3.385 | 3.534 | 3.696 | 3.870 | 4.057 | 4.135 | 4.216 | 4.298 | 4.382 |
| 1.6 | 3.326 | 3.463 | 3.616 | 3.786 | 3.973 | 4.175 | 4.394 | 4.630 | 4.728 | 4.830 | 4.934 | 5.040 |
| 1.8 | 3.658 | 3.815 | 3.994 | 4.194 | 4.417 | 4.661 | 4.927 | 5.215 | 5.336 | 5.461 | 5.589 | 5.721 |
| 2.0 | 3.985 | 4.162 | 4.367 | 4.600 | 4.861 | 5.149 | 5.465 | 5.809 | 5.954 | 6.104 | 6.258 | 6.416 |

The isotropic indentation moduli determined by applying the novel scaling factors approached the moduli calculated from unconfined compression tests of bovine cartilage samples, as compared to the indentation moduli determined using the Hayes' scaling factors (fig. 6.1). The improvement in the correspondence of the moduli was significant ($p < 0.0001$, fig. 6.2). However, significant ($p < 0.05$) differences were still observed between the indentation and unconfined compression moduli, as well as between the indenters (figs. 6.2 and 6.3, Study I: table 1).

**Table 6.2:** Novel scaling factors for the 3mm diameter indenter that was introduced in study I (see table 5.2).

| | **effective Poisson's ratio ($\nu_{eff}$)** | | | | | | | | | | | |
|---|---|---|---|---|---|---|---|---|---|---|---|---|
| $a/h$ | 0.05 | 0.10 | 0.15 | 0.20 | 0.25 | 0.30 | 0.35 | 0.40 | 0.42 | 0.44 | 0.46 | 0.48 |
| 0.2 | 1.421 | 1.446 | 1.457 | 1.454 | 1.436 | 1.404 | 1.357 | 1.296 | 1.267 | 1.237 | 1.203 | 1.168 |
| 0.4 | 1.684 | 1.682 | 1.677 | 1.669 | 1.658 | 1.645 | 1.629 | 1.610 | 1.602 | 1.593 | 1.584 | 1.574 |
| 0.6 | 1.928 | 1.931 | 1.937 | 1.947 | 1.960 | 1.976 | 1.996 | 2.019 | 2.029 | 2.040 | 2.051 | 2.063 |
| 0.8 | 2.187 | 2.207 | 2.235 | 2.270 | 2.313 | 2.364 | 2.422 | 2.487 | 2.515 | 2.545 | 2.575 | 2.607 |
| 1.0 | 2.463 | 2.505 | 2.558 | 2.623 | 2.700 | 2.788 | 2.888 | 2.999 | 3.047 | 3.097 | 3.148 | 3.202 |
| 1.2 | 2.752 | 2.818 | 2.899 | 2.996 | 3.109 | 3.237 | 3.381 | 3.541 | 3.609 | 3.680 | 3.754 | 3.829 |
| 1.4 | 3.055 | 3.145 | 3.254 | 3.384 | 3.534 | 3.703 | 3.893 | 4.102 | 4.191 | 4.284 | 4.379 | 4.478 |
| 1.6 | 3.365 | 3.481 | 3.620 | 3.784 | 3.972 | 4.183 | 4.419 | 4.679 | 4.789 | 4.904 | 5.022 | 5.144 |
| 1.8 | 3.686 | 3.823 | 3.989 | 4.184 | 4.410 | 4.664 | 4.948 | 5.262 | 5.396 | 5.534 | 5.678 | 5.825 |
| 2.0 | 4.011 | 4.169 | 4.362 | 4.590 | 4.854 | 5.153 | 5.487 | 5.856 | 6.013 | 6.177 | 6.345 | 6.520 |

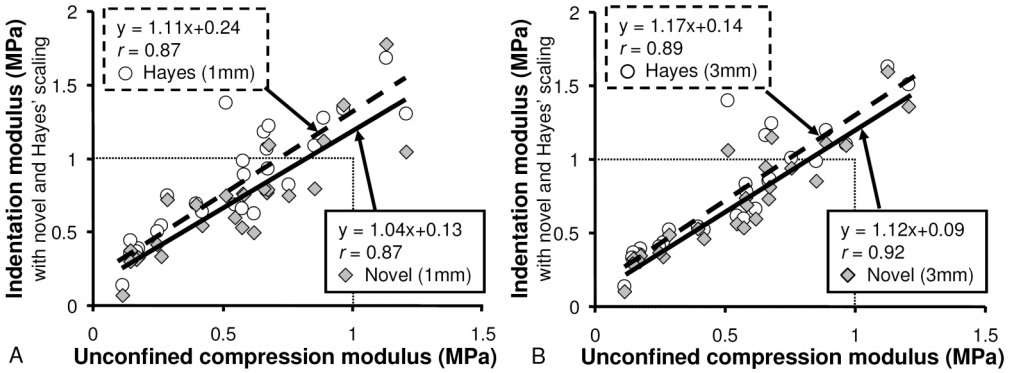


**Figure 6.1:** Scatter plots of unconfined compression modulus vs. indentation modulus. Indentation modulus was determined both using the novel scaling factors and using the Hayes' scaling factors with eq. 5.4. Indentation moduli are shown for indenters of 1mm (A) and 3mm (B) in diameter (study I). The novel scaling factors were determined with FRPVE model of unchanging structure, while the scaling factors were validated using experimental tests of cartilage samples.

Compression velocity significantly affected the peak forces during the stress-relaxation tests (Study I: fig. 4). With low compression velocities, highest peak forces were measured for the thickest cartilage (lowest aspect ratio). With high compression velocities, the subchondral bone increased especially the peak forces of the thin samples (high aspect ratio, Study I: figs. 4 and 5).

The Benninghoff-type collagen architecture was observed to play an important role in the detected reaction forces in indentation (Study I: fig. 6). The lowest equilibrium and peak forces were revealed with a homogeneous collagen architecture only consisting of vertical collagen fibrils. The highest equilibrium and peak forces were observed in the model with thick middle and superficial zones, 50% of the total cartilage thickness each.

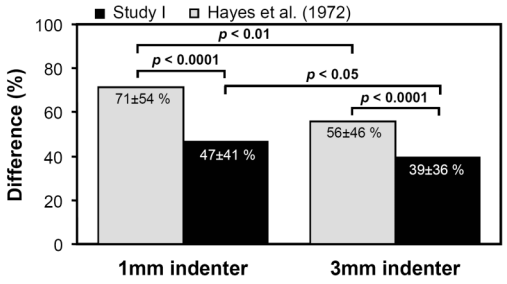


**Figure 6.2:** Difference between the unconfined compression modulus and the indentation modulus computed using the scaling factors introduced by Hayes et al. [53] and those presented in study I. Data from three joint sites were pooled.

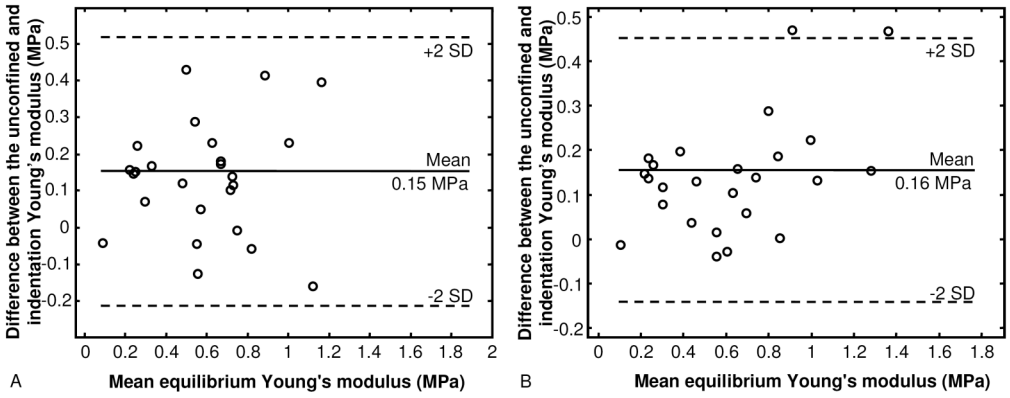


**Figure 6.3:** Bland-Altman plots for the agreement between the measured unconfined compression modulus and indentation moduli determined with 1 mm (A) and 3 mm (B) diameter indenters.

## 6.2 Relationships between imaging parameters and mechanical properties

The fibril moduli of cartilage correlated significantly ($p < 0.01$) and positively with the collagen content, as assessed from FT-IRIS (Study II: fig. 3). However, the initial collagen fibril modulus showed low negative or positive correlation ($p \leq 0.05$) with the T2 relaxation time for human or bovine cartilage, respectively (Study III: fig. 2).

The non-fibrillar matrix modulus showed a significant ($p < 0.05$) negative correlation with the T1 relaxation time and a significant positive correlation ($p < 0.001$) with the PG content, as measured with DD (Study III: fig. 1). The permeability constant $M$ showed a significant ($p < 0.01$) correlation with the PG content, and the initial permeability $k_0$ correlated significantly ($p < 0.01$) with the collagen content (Study II: fig. 5). The initial permeability also correlated with the T1 relaxation time ($r = 0.45$, $p < 0.05$). Compositional and structural parameters as

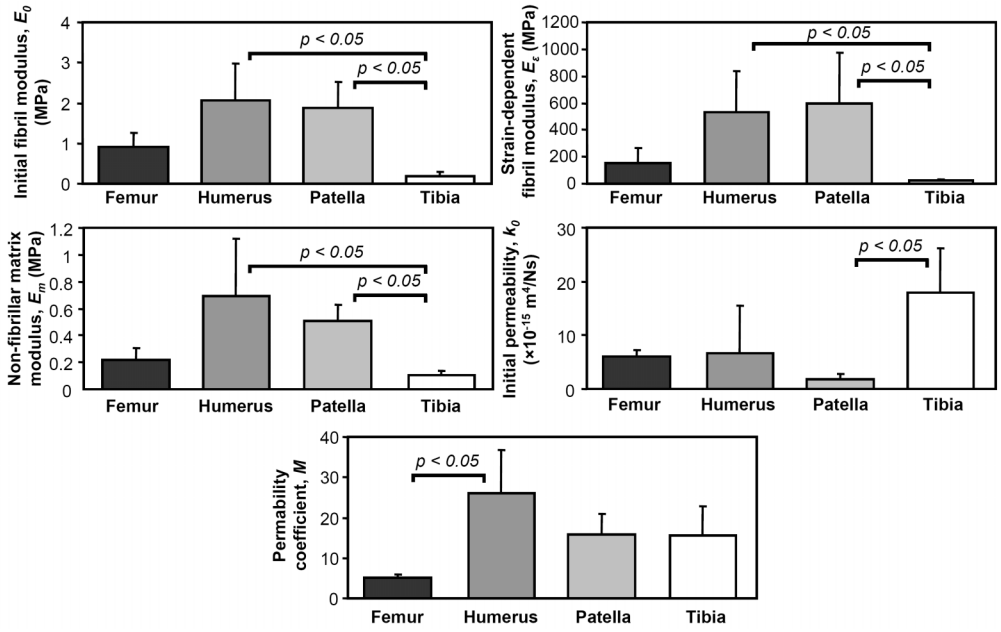


**Figure 6.4:** Site-specific model parameters in study II.

well as model parameters revealed significant ($p < 0.05$) site-specific differences (fig. 6.4).

## 6.3 MRI T2 and cartilage function

The effect of complex collagen architecture (3-7 laminae), as obtained from MRI T2, on the stress-relaxation response of cartilage was significant. Increases of 30.4% and 39.6% were observed in the detected peak reaction forces in the models with five and seven laminae collagen architectures, respectively, as compared to the model with a three laminae, Benninghoff-type architecture. Stress and strain distributions of the models with different collagen architectures revealed clear differences (fig. 6.5). The extra laminae increased local stresses and decreased lateral strains. The tensile logarithmic fibril strain ($\epsilon_f$, eq. 3.11) was larger in the vicinity of the extra laminae with horizontal collagen fibrils.

## 6.4 Estimation of cartilage function without mechanical testing

The composition-based fibril-reinforced model with a single set of optimized mechanical model properties was able to capture simultaneously stress-relaxation responses of three human articular cartilage samples under unconfined compression (fig. 6.6). The fitted values of the model parameters were: $E_1 = 6.632$ MPa, $E_2 = 15.555$ MPa, $k_1 = 3.825$, $k_2 = 72.328$, $n_0 = 1197.1$ MPa s, $\alpha = 5.127{\cdot}10^{17}\mathrm{m}^4/\mathrm{Ns}$. The average mean squared errors for the three samples were 0.6-7.6% with the correlation coefficient range of 0.95-0.99.

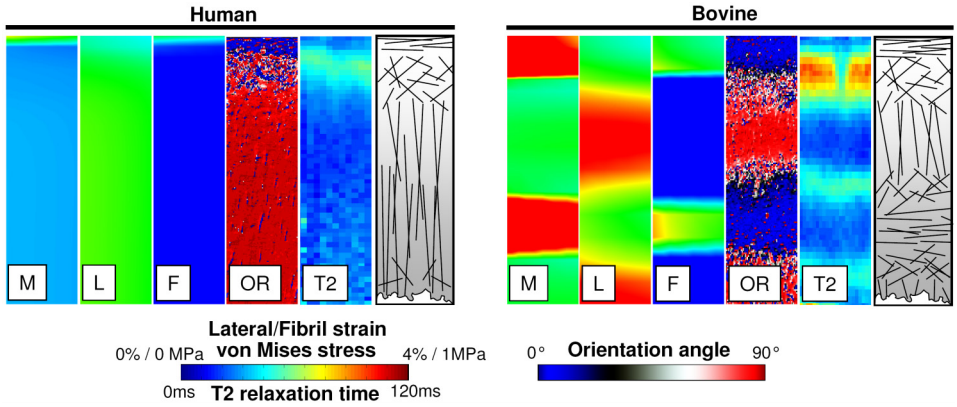


**Figure 6.5:** The effect of complex collagen architecture on stress/strain distributions in cartilage under 10% surface-to-surface strain in unconfined compression. Lateral nominal strain (L), tensile logarithmic fibril strain (F) and von Mises stress (M) distributions for samples with three laminae and seven laminae collagen architecture are presented in 10% surface-to-surface axial compression. For both samples, orientation (OR) distribution from PLM and spatial T2 distribution from MRI are also presented (assessed under unstrained conditions). Illustration showing the collagen arrangement in both samples is presented on the right.

Using the above-mentioned mechanical parameters and the experimentally determined tissue composition and structure, we were able to successfully predict the stress-relaxation responses of two additional human patellar cartilage samples in unconfined compression (fig. 6.6). The mean squared errors between simulations and experimental reaction forces were 2.2-12.5% with a correlation coefficient of 0.98 in both simulations.

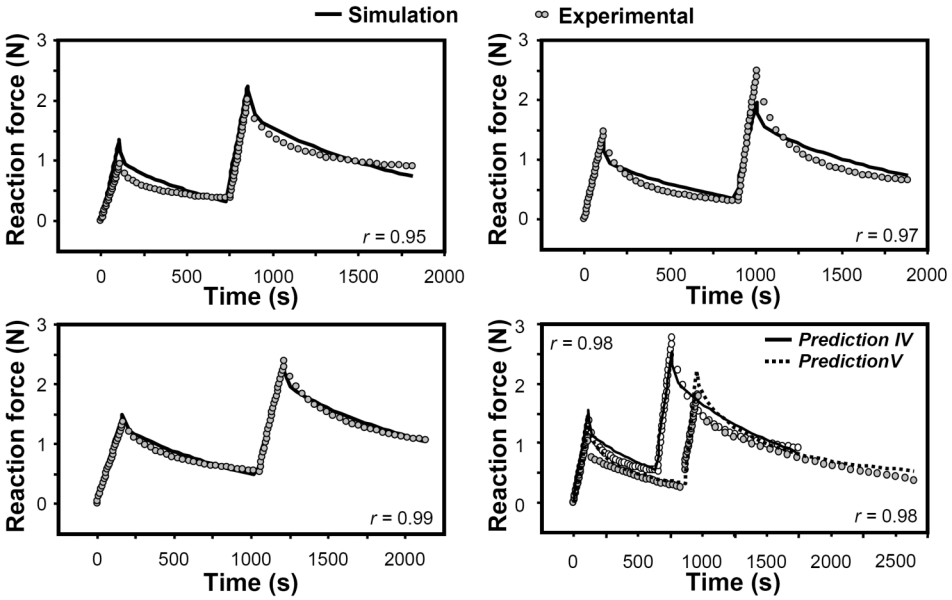


**Figure 6.6:** Experimental and simulated reaction forces in the mechanical stress-relaxation tests of five human cartilage samples. The mechanical model parameters were first obtained by fitting three models with sample-specific tissue composition and structure simultaneously to the experimental data. Then, by using the fitted mechanical parameters, the stress-relaxation curves of the validation samples were predicted using the sample-specific tissue composition and structure only.

Chapter VII

# Discussion

## 7.1 Tissue inhomogeneity and measurement geometry

The inhomogeneous collagen network structure affected significantly the mechanical response of articular cartilage. Minor variations in the Benninghoff-like arcade structure were observed to influence slightly the induced reaction forces in unconfined compression, whereas during indentation the effect of the collagen architecture was more emphasized (study I). When taking the inhomogeneity into account in the finite element simulations, the novel scaling factors improved the accuracy in the assessment of elastic cartilage properties in the indentation (fig. 6.2).

Significant species-specific variations were detected in the inhomogeneous collagen architecture (study III). The multilaminar collagen architecture, which may be a result of an early maturation process [74, 140, 144], altered significantly the stress-relaxation response of cartilage. Based on our findings, we postulate that it is essential to take account of the effect of the actual collagen architecture while assessing the mechanical condition of the cartilage collagen, since the fibril orientation itself contributes to the mechanical response of the tissue.

The collagen architecture was shown to affect both the equilibrium and peak responses of cartilage, which increased significantly as the superficial zone thickness increased, also observed by Korhonen et al. [83]. Thus, implementation of a sample-specific collagen architecture into the model improved the correspondence in the moduli calculated from indentation and unconfined compression. Surprisingly, it was observed that also the middle zone contributed to the indentation response, especially under conditions of instantaneous compression. This was likely due to the fact that under compression, the more randomly oriented fibrils in the middle zone, aligned towards a parallel-to-surface orientation, and increased the effective thickness of the superficial zone [2]. Thus, this increased the tensile stiffness of the superficial layers of cartilage. Furthermore, FCD and water might affect the mechanical response of the tissue especially during indentation [5, 101, 102, 143], which was not tested here (study I).

During the preparation of sample plugs for unconfined compression, the biopsy punch induces local collagen damage on the sample edges [83]. This may have had some influence on the analysis of the fibril network modulus, possibly inducing some discrepancies between the fibril network moduli obtained from indentation and unconfined compression. This may partly explain why the indentation moduli were systematically higher than the moduli determined from unconfined compression.

## 7.2 Swelling

In studies I-III, osmotic swelling was not included, since the intent was to simulate reaction forces while optimizing the FRPVE model parameters. Instead, the effects of osmotic swelling were taken into account in the non-fibrillar matrix modulus. Furthermore, sensitivity analysis (Study IV: fig. 5) indicated that the changes in FCD and swelling would not change reaction forces significantly in unconfined compression geometry. However, this may not be the case in other loading geometries and protocols. In study IV, osmotic swelling was necessary for the composition-based simulations.

## 7.3 Interrelations between imaging parameters and mechanical properties

Inter-relations between the FT-IRIS-derived collagen content and collagen network moduli suggested that the apparent mechanical stiffness of the collagen network increases as the collagen content per sample volume increases. This is consistent with the dynamic modulus - collagen content relationship. It is known that the collagen network together with fluid pressurization modulates the instantaneous response [95]. Therefore, one may assume a relation between the dynamic modulus and collagen fibril modulus. Thus, our results correspond well with the earlier findings [68, 74, 119]. However, the dynamic and collagen fibril modulus are not equivalent. The collagen fibril modulus describes only the mechanical properties of the collagen network, whereas the dynamic modulus reflects the mechanical properties of the entire tissue.

Initial tissue permeability was shown to depend inversely on the collagen content, which agrees with earlier studies [45, 80, 113]. It is likely that the tight packing of the collagen fibrils induces thinner paths for the interstitial fluid flow, probably due to the more closely packed GAG chains, decreasing the tissue permeability [80, 113]. Also, permeability has earlier been shown to depend on the tissue FCD [111]. Since FCD is mainly a result from negatively charged PGs, the presented dependence between the PG content and permeability coefficient ($M$) is in agreement with the results presented by Maroudas et al. [111]. In the model, $M$ describes the relation between permeability and void ratio (eq. 3.5), which is known to be related to the PG content [98, 181, 190, 191].

Equilibrium Young's modulus has been shown to be related to the PG content (derived using DD) of cartilage [74, 80, 86, 117]. In addition, FT-IRIS derived PG content has been shown to correlate with the equilibrium Young's modulus [148]. The results presented in this thesis for the inter-relations between the non-fibrillar matrix modulus and PG content are in good agreement with those from earlier studies [74, 80, 86, 117]. However, as the collagen network also contributes to the equilibrium response [69, 80], the non-fibrillar matrix modulus should not be directly compared with the equilibrium Young's modulus. The separation of the non-fibrillar matrix from the fibrillar matrix provides a measure, which is mainly descriptive of the mechanical properties of tissue PGs. The non-fibrillar matrix modulus includes the effects of swelling in equilibrium, since the equilibrium strength of the PGs results from FCD, which attracts fluid [29, 35].

The significant negative correlation between the T1 relaxation time and the non-fibrillar matrix modulus is in agreement with previous studies [84, 124, 186]. We found that the initial permeability is also related to T1, which suggests that PGs are mainly responsible for the fluid flow characteristics in cartilage. These results support earlier findings that T1 could be a sensitive parameter for describing PG loss during spontaneous degeneration of cartilage

[126, 184], i.e. a decrease of the cartilage stiffness and an increase of the permeability occur in osteoarthritis [155].

The correlation between T2 and the dynamic modulus has earlier been shown to be either negative or positive [84, 124]. There are still no clear explanations to account for these discrepancies. A high T2 value reflects a disorganized and structurally isotropic collagen network, and was hypothesized to increase, as the dynamic or collagen network modulus decreases. In this thesis, in accordance with an earlier study [84], this behavior was observed in human patellae, which have an arcade-like collagen architecture with three laminae [17]. In contrast, the results for bovine samples implied a positive correlation between T2 and the collagen network modulus, as observed experimentally between T2 and the dynamic modulus by Nieminen et al. [124]. It is suggested that the extra laminae found in bovine cartilage increases the bulk T2 value, due to increased anisotropy of the collagen fibrils in the deep zone. At the same time, due to the collagen orientation of 0-45 degrees in the extra layers, the peak force of the stress-relaxation tests increases, leading to higher values of the dynamic or collagen network modulus and positive correlation between T2 and the fibril moduli. Due to the varying collagen architecture of articular cartilage, its effect on the MRI T2 must be acknowledged.

In study IV, mechanical behavior of articular cartilage was predicted based on tissue composition only. This is based on the compositional analysis of water, PGs and collagen, which do not distinguish the subgroups of these constituents. The effect of different collagen subtypes on the mechanical behavior of the collagen network may well vary, but their implementation in the applied composition-based model is the same. Therefore, the collagen in the composition-based model represents the total effect of all subtypes that are present in the specimen. The predominant collagen in articular cartilage is type II. However, the role of other collagen types may become important in OA, if their proportion in the total collagen content becomes altered [54, 151]. Similarly, other factors like crosslink density, GAG length and cell density might have an effect on the mechanical response [27, 41, 51, 159, 183], but this cannot be distinctively quantified through FT-IRIS analysis or be implemented into the model. Although all these factors may affect the mechanical behavior of articular cartilage, the predominant effect of the basic cartilage constituents, independent of subtypes, is seen through the applied compositional and structural analyses (fig. 6.6). However, the mentioned factors should be considered to cause measurement error in compositional analysis, as well as some error in the composition-based prediction of mechanical behavior. Therefore, the sensitivity of the composition-based theory to detect early changes in OA needs to be further validated in the future with samples developing OA.

## 7.4 Values of material parameters

In the present thesis, the mechanical properties of cartilage components (collagen and PGs) were determined using a fibril reinforced poroviscoelastic FE model. In addition, fluid flow properties of cartilage were determined. The values for the collagen fibril moduli were similar to those reported earlier [80, 98, 191]. The permeability values were in good agreement with the earlier experimental and FE studies [12, 80, 82, 90, 93, 109, 185, 188, 189, 190, 191]. Topographical and species-specific variations in the moduli ($E_0$, $E_\epsilon$ and $E_m$) were similar to those presented earlier [88].

The values of the non-fibrillar matrix moduli were lower than the equilibrium Young's modulus values presented in earlier studies [74, 128]. This is explained by the collagen network affecting the elastic/equilibrium Young's modulus of cartilage [80]. The non-fibrillar matrix

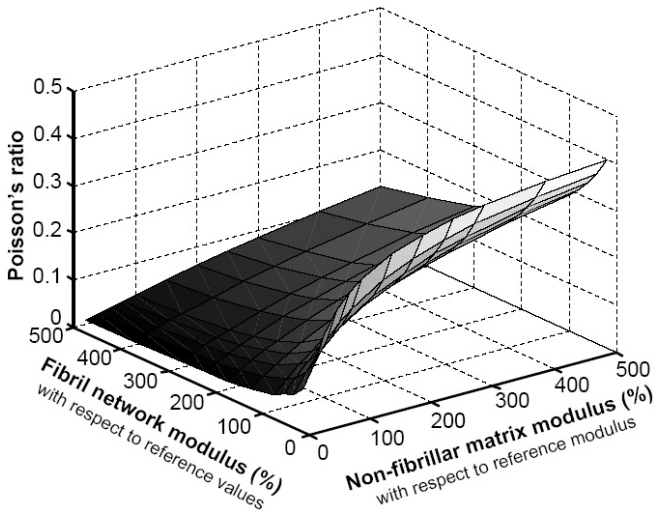


**Figure 7.1:** The effect of the non-fibrillar matrix modulus ($E_m$) and fibril network modulus on the effective Poisson's ratio ($\nu_{eff}$) of cartilage. The modulus values are presented with respect to the reference values. The reference value (100%) of the non-fibrillar matrix modulus was 0.31 MPa. The reference values (100%) of the fibril network modulus were presented with three parameters: $E_0 = 0.47$ MPa, $E_\epsilon = 673$ MPa and $\eta = 947$ MPa·s. The Poisson's ratio of the non-fibrillar matrix ($\nu_m$) was fixed to 0.42 [98]

modulus depends almost entirely on the properties of PG, whereas the equilibrium Young's modulus also reflects the equilibrium tension state of collagen matrix.

It was confirmed that the collagen network is mainly responsible for the Poisson's ratio of cartilage (fig. 7.1) [64, 74]. The non-fibrillar matrix Young's modulus had a lower impact on the values of the cartilage Poisson's ratio. However, the Poisson's ratio of the non-fibrillar matrix influenced the effective Poisson's ratio significantly. Therefore, the dependence between the effective and non-fibrillar matrix Poisson's ratios was assumed (eq. 5.1). According to the simulations of the effective Poisson's ratio, the presented dependence was shown to be valid. However, since both the fibrillar and non-fibrillar matrix affect the effective Poisson's ratio, the dependence is only an approximation. In studies I-III, the Poisson's ratio of the non-fibrillar matrix had to be estimated either with the linear approximation from the measured effective Poisson's ratio (eq. 5.1, study II), or based on the literature (studies I and III). Instead, a different approach such as modeling the non-fibrillar matrix Poisson's ratio based on solid volume fraction (eq. 3.9) [189], or modeling the non-fibrillar matrix (mainly PGs) as a gel [29, 137], could be used without having to resort to a non-physiological value for the non-fibrillar matrix Poisson's ratio.

In studies II and III, the viscoelastic damping coefficient of collagen fibrils was fixed. This was justified as the flow-independent viscoelasticity of the collagen fibrils has been earlier shown to have a negligible influence on the measured reaction forces in compression [96]. However, with viscoelastic behavior implemented for the collagen fibrils, the time-dependent lateral deformation can be simulated in a realistic manner (Study III, fig. 5) [44, 190, 191]. Thus, this

property was implemented into the models.

The composition-based model theory applied in study IV was introduced recently; however, its applicability was demonstrated without sample-specific composition and structure that were implemented from earlier experimental studies on bovine cartilage [188, 189]. In those studies, the composition-based model predicted the mechanical behavior successfully in several loading geometries, but it was not validated with sample-specific compositional data. In addition, different samples were used for all the test geometries. These were the major limitations of the previous study [188] that were overcome in the present work (study IV). For these reasons, the optimized values for model parameters presented in study IV are different from those presented earlier by Wilson et al. [188] for bovine cartilage (Study IV: table 2). For general use of the model in simulating transient mechanical behavior of articular cartilage based on tissue composition and structure, the composition-based model needs to be further validated and developed for other loading geometries, and in three-dimensional geometry for modeling joint mechanics.

Chapter VIII

# Summary and Conclusions

The present thesis used microstructural modeling and mechanical testing to investigate the mechanical characteristics of cartilage tissue components, i.e. collagen, PGs and fluid, their relationships to structure and composition of cartilage, and especially the effects of structure and composition on tissue function. Further, the potential of using composition-based modeling to predict the time-dependent mechanical response of cartilage under compression, based on data of composition only, was assessed. Assessment of the elastic properties of articular cartilage was evaluated through (clinically applicable) indentation and microstructural modeling.

The main findings and conclusions of the present study are listed below:

- The collagen network architecture and thickness of articular cartilage as well as the compression rate are important factors to be taken into account in the analysis of the indentation modulus, especially during instantaneous compression.
- This study provided a simple alternative solution for the indentation problem by introducing novel scaling factors to be used with the Hayes' solution [53], resulting in a more accurate estimation of the Young's modulus of articular cartilage from indentation tests.
- When combined with the FRPVE model, the modern microscopic methods are feasible methods to address structure-function relationships in articular cartilage. It may be possible to predict the collagen fibril modulus, non-fibrillar matrix modulus and permeability without mechanical testing.
- PG sensitive mechanical properties of articular cartilage, i.e. the non-fibrillar matrix modulus and the initial permeability, may be assessed with the T1 relaxation time of MRI.
- The relationship between the T2 relaxation time and the collagen stiffness is very complicated. Therefore, a depth-dependent analysis of the collagen architecture is needed in the evaluation of cartilage quality by MRI T2.
- Since it takes into account the sample-specific tissue composition and structure, the theoretical model was able to capture the compressive stress-relaxation behavior of human articular cartilage under unconfined compression implying that cartilage function can be predicted without mechanical testing. Previously, these kinds of predictions have not been made successfully with other models for articular cartilage.

## 8.1 Novel techniques for functional imaging?

In the future, valuable new information on the development of articular cartilage and the etiology of OA may be obtained by combining FE methods with quantitative imaging techniques. These may be very useful in the early detection of OA. In addition, by using composition-based modeling, it may be possible to assess the mechanical properties of cartilage providing a path from quantitative imaging, such as MRI, to cartilage function. This kind of functional imaging may well represent a sensitive technique to characterize the effect of loading on stresses and strains in healthy and OA cartilage. Furthermore, it may reveal possible failure points in joints, or indicate the effect of joint misalignment on peak stresses in cartilage. This would provide new tools for use in the clinic, e.g. when planning surgical treatments for OA patients.

1. Alexopoulos L. G., Williams G. M., Upton M. L., Setton L. A. and Guilak F. Osteoarthritic changes in the biphasic mechanical properties of chondrocyte pericellular matrix in articular cartilage. *J Biomech*, 38(3):509–17, 2005.

2. Alhadlaq H. A. and Xia Y. The structural adaptations in compressed articular cartilage by microscopic MRI (microMRI) T(2) anisotropy. *Osteoarthritis Cartilage*, 12(11):887–94, 2004.

3. Alhadlaq H. A., Xia Y., Moody J. B. and Matyas J. R. Detecting structural changes in early experimental osteoarthritis of tibial cartilage by microscopic magnetic resonance imaging and polarised light microscopy. *Ann Rheum Dis*, 63(6):709–17, 2004.

4. ap Gwynn I., Wade S., Ito K. and Richards R. G. Novel aspects to the structure of rabbit articular cartilage. *Eur Cell Mater*, 4:18–29, 2002.

5. Appleyard R. C., Burkhardt D., Ghosh P., Read R., Cake M., Swain M. V. and Murrell G. A. Topographical analysis of the structural, biochemical and dynamic biomechanical properties of cartilage in an ovine model of osteoarthritis. *Osteoarthritis Cartilage*, 11(1):65–77, 2003.

6. Appleyard R. C., Swain M. V., Khanna S. and Murrell G. A. The accuracy and reliability of a novel handheld dynamic indentation probe for analysing articular cartilage. *Phys Med Biol*, 46(2):541–50, 2001.

7. Armstrong C. G. and Mow V. C. Variations in the intrinsic mechanical properties of human articular cartilage with age, degeneration, and water content. *J Bone Joint Surg Am*, 64(1):88–94, 1982.

8. Arokoski J., Jurvelin J., Kiviranta I., Tammi M. and Helminen H. J. Softening of the lateral condyle articular cartilage in the canine knee joint after long distance (up to 40 km/day) running training lasting one year. *Int J Sports Med*, 15(5):254–60, 1994.

9. Arokoski J. P., Hyttinen M. M., Lapveteläinen T., Takacs P., Kosztaczky B., Modis L., Kovanen V. and Helminen H. Decreased birefringence of the superficial zone collagen network in the canine knee (stifle) articular cartilage after long distance running training, detected by quantitative polarised light microscopy. *Ann Rheum Dis*, 55(4):253–64, 1996.

10. Arokoski J. P., Jurvelin J. S., Väätäinen U. and Helminen H. J. Normal and pathological adaptations of articular cartilage to joint loading. *Scand J Med Sci Sports*, 10(4):186–98, 2000.

11. Aspden R. M. and Hukins D. W. Collagen organization in articular cartilage, determined by X-ray diffraction, and its relationship to tissue function. *Proc R Soc Lond B Biol Sci*, 212(1188):299–304, 1981.

12. Ateshian G. A., Warden W. H., Kim J. J., Grelsamer R. P. and Mow V. C. Finite deformation biphasic material properties of bovine articular cartilage from confined compression experiments. *J Biomech*, 30(11-12):1157–64, 1997.

13. Bachrach N. M., Valhmu W. B., Stazzone E., Ratcliffe A., Lai W. M. and Mow V. C. Changes in proteoglycan synthesis of chondrocytes in articular cartilage are associated with the time-dependent changes in their mechanical environment. *J Biomech*, 28(12):1561–9, 1995.

14. Bae W. C., Wong V. W., Hwang J., Antonacci J. M., Nugent-Derfus G. E., Blewis M. E., Temple-Wong M. M. and Sah R. L. Wear-lines and split-lines of human patellar cartilage: relation to tensile biomechanical properties. *Osteoarthritis Cartilage*, 16(7):841–5, 2008.

15. Bank R. A., Soudry M., Maroudas A., Mizrahi J. and TeKoppele J. M. The increased swelling and instantaneous deformation of osteoarthritic cartilage is highly correlated with collagen degradation. *Arthritis Rheum*, 43(10):2202–10, 2000.

16. Basser P. J., Schneiderman R., Bank R. A., Wachtel E. and Maroudas A. Mechanical properties of the collagen network in human articular cartilage as measured by osmotic stress technique. *Arch Biochem Biophys*, 351(2):207–19, 1998.

17. Benninghoff A. Form und Bau der Gelenkknorpel in ihren Beziehungen zur Function. *Zeitschrift für Zellforschung*, 2:783–862, 1925.

18. Bi X., Li G., Doty S. B. and Camacho N. P. A novel method for determination of collagen orientation in cartilage by Fourier transform infrared imaging spectroscopy (FT-IRIS). *Osteoarthritis Cartilage*, 13(12):1050–8, 2005.

19. Bi X., Yang X., Bostrom M. P., Bartusik D., Ramaswamy S., Fishbein K. W., Spencer R. G. and Camacho N. P. Fourier transform infrared imaging and MR microscopy studies detect compositional and structural changes in cartilage in a rabbit model of osteoarthritis. *Anal Bioanal Chem*, 387(5):1601–12, 2007.

20. Bi X., Yang X., Bostrom M. P. and Camacho N. P. Fourier transform infrared imaging spectroscopy investigations in the pathogenesis and repair of cartilage. *Biochim Biophys Acta*, 1758(7):934–41, 2006.

21. Blair-Levy J. M., Watts C. E., Fiorientino N. M., Dimitriadis E. K., Marini J. C. and Lipsky P. E. A type I collagen defect leads to rapidly progressive osteoarthritis in a mouse model. *Arthritis Rheum*, 58(4):1096–106, 2008.

22. Blumenkrantz N. and Asboe-Hansen G. New method for quantitative determination of uronic acids. *Anal Biochem*, 54(2):484–9, 1973.

23. Brown S., Worsfold M. and Sharp C. Microplate assay for the measurement of hydroxyproline in acid-hydrolyzed tissue samples. *Biotechniques*, 30(1):38–40, 42, 2001.

24. Buckwalter J. A. and Martin J. Degenerative joint disease. *Clin Symp*, 47(2):1–32, 1995.

25. Buckwalter J. A., Mow V. C. and Ratcliffe A. Restoration of Injured or Degenerated Articular Cartilage. *J Am Acad Orthop Surg*, 2(4):192–201, 1994.

26. Buckwalter J. A., Rosenberg L. C. and Hunziker E. B. Articular cartilage: Composition, structure, response to injury, and methods of facilitating repair. In Ewing J. W., editor, *Articular cartilage and knee joint function: Basic science and arthroscopy*, pages 19–56. Raven Press, Ltd., New York, 1990.

27. Buckwalter J. and Mankin H. Articular Cartilage, Part II: Degeneration and osteoarthritis, repair, regeneration, and transplantation. *J Bone Joint Surg Am*, 79(4):612–32, 1997.

28. Buschmann M. D., Gluzband Y. A., Grodzinsky A. J. and Hunziker E. B. Mechanical compression modulates matrix biosynthesis in chondrocyte/agarose culture. *J Cell Sci*, 108(Pt 4):1497–508, 1995.

29. Buschmann M. D. and Grodzinsky A. J. A molecular model of proteoglycan-associated electrostatic forces in cartilage mechanics. *J Biomech Eng*, 117(2):179–92, 1995.

30. Camacho N. P., West P., Torzilli P. A. and Mendelsohn R. FTIR microscopic imaging of collagen and proteoglycan in bovine cartilage. *Biopolymers*, 62(1):1–8, 2001.

31. Clark A. L., Barclay L. D., Matyas J. R. and Herzog W. In situ chondrocyte deformation with physiological compression of the feline patellofemoral joint. *J Biomech*, 36(4):553–68, 2003.

32. Clark A. L., Leonard T. R., Barcley L. D., Matyas J. R. and Herzog W. Opposing cartilages in the patellofemoral joint adapt differently to long-term cruciate deficiency: chondrocyte deformation and reorientation with compression. *Osteoarthritis Cartilage*, 13:1100–14, 2005.

33. Cohen B., Lai W. M. and Mow V. C. A transversely isotropic biphasic model for unconfined compression of growth plate and chondroepiphysis. *J Biomech Eng*, 120(4):491–6, 1998.

34. DiSilvestro M. R., Zhu Q., Wong M., Jurvelin J. S. and Suh J. K. Biphasic poroviscoelastic simulation of the unconfined compression of articular cartilage: I–Simultaneous prediction of reaction force and lateral displacement. *J Biomech Eng*, 123(2):191–7, 2001.

35. Eisenberg S. R. and Grodzinsky A. J. Swelling of articular cartilage and other connective tissues: electromechanochemical forces. *J Orthop Res*, 3(2):148–59, 1985.

36. Eyre D. Collagen of articular cartilage. *Arthritis Res*, 4(1):30–5, 2002.

37. Eyre D. R., Dickson I. R. and Van Ness K. Collagen cross-linking in human bone and articular cartilage. Age- related changes in the content of mature hydroxypyridinium residues. *Biochem J*, 252(2):495–500, 1988.

38. Eyre D. R., Wu J. J. and Apone S. A growing family of collagens in articular cartilage: identification of 5 genetically distinct types. *J Rheumatol*, 14 Spec No:25–7, 1987.

39. Fairbank T. J. Knee joint changes after meniscectomy. *J Bone Joint Surg Br*, 30-B(4):664–70, 1948.

40. Federico S. and Herzog W. On the anisotropy and inhomogeneity of permeability in articular cartilage. *Biomech Model Mechanobiol*, 2007, in press.

41. Federico S., Herzog W., Wu J. Z. and La Rosa G. A method to estimate the elastic properties of the extracellular matrix of articular cartilage. *J Biomech*, 37(3):401–4, 2004.

42. Garcia J. J., Altiero N. J. and Haut R. C. An approach for the stress analysis of transversely isotropic biphasic cartilage under impact load. *J Biomech Eng*, 120(5):608–13, 1998.

43. Garcia J. J., Altiero N. J. and Haut R. C. Estimation of in situ elastic properties of biphasic cartilage based on a transversely isotropic hypo-elastic model. *J Biomech Eng*, 122(1):1–8, 2000.

44. Garcia J. J. and Cortés D. H. A Biphasic viscoelastic fibril-reinforced model for articular cartilage: Formulation and comparison with experimental data. *J Biomech*, 40(8):1737–44, 2007.

45. Garon M., Légaré A., Quenneville E., Hurtig M. B. and Buschmann M. D. Streaming potential based arthroscopic instrument distinguishes site-specific properties of equine articular cartilage. In *Trans Orthop Res Soc*, volume 28, page 255, 2003.

46. Gray M. L., Burstein D. and Xia Y. Biochemical (and functional) imaging of articular cartilage. *Semin Musculoskelet Radiol*, 5(4):329–43, 2001.

47. Grunder W., Kanowski M., Wagner M. and Werner A. Visualization of pressure distribution within loaded joint cartilage by application of angle-sensitive NMR microscopy. *Magn Reson Med*, 43(6):884–91, 2000.

48. Gu W. Y., Lai W. M. and Mow V. C. Transport of fluid and ions through a porous-permeable charged-hydrated tissue, and streaming potential data on normal bovine articular cartilage. *J Biomech*, 26(6):709–23, 1993.

49. Gu W. Y., Lai W. M. and Mow V. C. A mixture theory for charged-hydrated soft tissues containing multi- electrolytes: passive transport and swelling behaviors. *J Biomech Eng*, 120(2):169–80, 1998.

50. Guilak F. The deformation behavior and viscoelastic properties of chondrocytes in articular cartilage. *Biorheology*, 37:27–44, 2000.

51. Guilak F., Ratcliffe A., Lane N., Rosenwasser M. P. and Mow V. C. Mechanical and biochemical changes in the superficial zone of articular cartilage in canine experimental osteoarthritis. *J Orthop Res*, 12(4):474–84, 1994.

52. Guilak F., Ratcliffe A. and Mow V. C. Chondrocyte deformation and local tissue strain in articular cartilage: a confocal microscopy study. *J Orthop Res*, 13(3):410–21, 1995.

53. Hayes W. C., Keer L. M., Herrmann G. and Mockros L. F. A mathematical analysis for indentation tests of articular cartilage. *J Biomech*, 5(5):541–51, 1972.

54. Helminen H. J., Saamanen A. M., Salminen H. and Hyttinen M. M. Transgenic mouse models for studying the role of cartilage macromolecules in osteoarthritis. *Rheumatology (Oxford)*, 41(8):848–56, 2002.

55. Hoch D. H., Grodzinsky A. J., Koob T. J., Albert M. L. and Eyre D. R. Early changes in material properties of rabbit articular cartilage after meniscectomy. *J Orthop Res*, 1(1):4–12, 1983.

56. Holmes M. H. and Mow V. C. The nonlinear characteristics of soft gels and hydrated connective tissues in ultrafiltration. *J Biomech*, 23(11):1145–56, 1990.

57. Hughes L. C., Archer C. W. and ap Gwynn I. The ultrastructure of mouse articular cartilage: collagen orientation and implications for tissue functionality. A polarized light and scanning electron microscope study and review. *Eur Cell Mater*, 9:68–84, 2005.

58. Hunziker E. B. Articular cartilage structure in humans and experimental animals. In Kuettner K., editor, *Articular cartilage and osteoarthritis*, pages 183–197. Raven Press, New York, 1992.

59. Huyghe J. M., Houben G. B., Drost M. R. and van Donkelaar C. C. An ionised/non-ionised dual porosity model of intervertebral disc tissue. *Biomech Model Mechanobiol*, 2(1):3–19, 2003.

60. Huyghe J. M. and Janssen J. D. Quadriphasic mechanics of swelling incompressible porous media. *Int J Eng Sci*, 35(8):793–802, 1997.

61. Jeffery A. K., Blunn G. W., Archer C. W. and Bentley G. Three-dimensional collagen architecture in bovine articular cartilage. *J Bone Joint Surg [Br]*, 73(5):795–801, 1991.

62. Jones I. L., Larsson S. E. and Lemperg R. The glycosaminoglycans of human articular cartilage: concentration and distribution in different layers in the adult individual. *Clin Orthop*, 127:257–64, 1977.

63. Julkunen P., Korhonen R. K., Nissi M. J. and Jurvelin J. S. Multilaminar collagen structure increases load-bearing capacity of articular cartilage. In *Trans Orthop Res Soc*, volume 32, page 604, 2007.

64. Jurvelin J. S., Arokoski J. P., Hunziker E. B. and Helminen H. J. Topographical variation of the elastic properties of articular cartilage in the canine knee. *J Biomech*, 33(6):669–75, 2000.

65. Jurvelin J. S., Buschmann M. D. and Hunziker E. B. Optical and mechanical determination of Poisson's ratio of adult bovine humeral articular cartilage. *J Biomech*, 30(3):235–41, 1997.

66. Kääb M. J., ap Gwynn I. and Nötzli H. P. Collagen fibre arrangement in the tibial plateau articular cartilage of man and other mammalian species. *J Anat*, 193:23–34, 1998.

67. Kääb M. J., Ito K., Rahn B., Clark J. M. and Nötzli H. P. Effect of mechanical load on articular cartilage collagen structure: a scanning electron-microscopic study. *Cells Tissues Organs*, 167(2-3):106–20, 2000.

68. Kempson G. E., Muir H., Pollard C. and Tuke M. The tensile properties of the cartilage of human femoral condyles related to the content of collagen and glycosaminoglycans. *Biochim Biophys Acta*, 297(2):456–72, 1973.

69. Khalsa P. S. and Eisenberg S. R. Compressive behavior of articular cartilage is not completely explained by proteoglycan osmotic pressure. *J Biomech*, 30(6):589–94, 1997.

70. Király K., Hyttinen M. M., Lapveteläinen T., Elo M., Kiviranta I., Dobai J., Modis L., Helminen H. J. and Arokoski J. P. Specimen preparation and quantification of collagen birefringence in unstained sections of articular cartilage using image analysis and polarizing light microscopy. *Histochem J*, 29(4):317–27, 1997.

71. Király K., Lapveteläinen T., Arokoski J., Törrönen K., Modis L., Kiviranta I. and Helminen H. J. Application of selected cationic dyes for the semiquantitative estimation of glycosaminoglycans in histological sections of articular cartilage by microspectrophotometry. *Histochem J*, 28(8):577–90, 1996.

72. Kiviranta I., Jurvelin J., Tammi M., Säämänen A. M. and Helminen H. J. Microspectrophotometric quantitation of glycosaminoglycans in articular cartilage sections stained with Safranin O. *Histochemistry*, 82(3):249–55, 1985.

73. Kiviranta P., Lammentausta E., Töyräs J., Kiviranta I. and Jurvelin J. S. Indentation diagnostics of cartilage degeneration. *Osteoarthritis Cartilage*, 16(7):796–804, 2008.

74. Kiviranta P., Rieppo J., Korhonen R. K., Julkunen P., Töyräs J. and Jurvelin J. S. Collagen network primarily controls the Poisson's ratio of bovine articular cartilage in compression. *J Orthop Res*, 24(4):690–9, 2006.

75. Kiviranta P., Töyräs J., Nieminen M. T., Laasanen M. S., Saarakkala S., Nieminen H. J., Nissi M. J. and Jurvelin J. S. Comparison of novel clinically applicable methodology for sensitive diagnostics of cartilage degeneration. *Eur Cell Mater*, 13:46–55, 2007.

76. Knecht S., Vanwanseele B. and Stüssi E. A review on the mechanical quality of articular cartilage - implications for the diagnosis of osteoarthritis. *Clin Biomech (Bristol, Avon)*, 21(10):999–1012, 2006.

77. Korhonen R. K. and Herzog W. Depth-dependent analysis of the role of collagen fibrils, fixed charges and fluid in the pericellular matrix of articular cartilage on chondrocyte mechanics. *J Biomech*, 41(2):480–5, 2007.

78. Korhonen R. K., Julkunen P., Rieppo J., Lappalainen R., Konttinen Y. T. and Jurvelin J. S. Collagen network of articular cartilage modulates fluid flow and mechanical stresses in chondrocyte. *Biomech Model Mechanobiol*, 5(2-3):150–9, 2006.

79. Korhonen R. K., Julkunen P., Wilson W. and Herzog W. Collagen network and fixed charge density of articular cartilage modulate time- and depth-dependent behavior of chondrocytes. *J Biomech Eng*, 130(2):021003, 2008.

80. Korhonen R. K., Laasanen M. S., Toyras J., Lappalainen R., Helminen H. J. and Jurvelin J. S. Fibril reinforced poroelastic model predicts specifically mechanical behavior of normal, proteoglycan depleted and collagen degraded articular cartilage. *J Biomech*, 36(9):1373–9, 2003.

81. Korhonen R. K., Laasanen M. S., Töyräs J., Helminen H. J. and Jurvelin J. S. Comparison of the equilibrium response of articular cartilage in unconfined compression, confined compression and indentation. *J Biomech*, 35(7):903–9, 2002.

82. Korhonen R. K., Saarakkala S., Töyräs J., Laasanen M. S., Kiviranta L. and Jurvelin J. S. Experimental and numerical validation for the novel configuration of an arthroscopic indentation instrument. *Phys Med Biol*, 48(11):1565–76, 2003.

83. Korhonen R. K., Wong M., Arokoski J., Lindgren R., Helminen H. J., Hunziker E. B. and Jurvelin J. S. Importance of the superficial tissue layer for the indentation stiffness of articular cartilage. *Med Eng Phys*, 24(2):99–108, 2002.

84. Kurkijärvi J. E., Nissi M. J., Kiviranta I., Jurvelin J. S. and Nieminen M. T. Delayed gadolinium-enhanced MRI of cartilage (dGEMRIC) and T2 characteristics of human knee articular cartilage: topographical variation and relationships to mechanical properties. *Magn Reson Med*, 52(1):41–6, 2004.

85. Kurkijärvi J. E., Nissi M. J., Rieppo J., Töyräs J., Kiviranta I., Nieminen M. T. and Jurvelin J. S. The zonal architecture of human articular cartilage described by T2 relaxation time in presence of Gd-DTPA2-. *Magn Reson Imaging*, 26(5):602–7, 2008.

86. Laasanen M., Saarakkala S., Töyräs J., Hirvonen J., Rieppo J., Korhonen R. K. and Jurvelin J. S. Ultrasound indentation of bovine articular cartilage in situ. *J Biomech*, 36:1259–67, 2003.

87. Laasanen M. S., Töyräs J., Hirvonen J., Saarakkala S., Korhonen R. K., Nieminen M. T., Kiviranta I. and Jurvelin J. S. Novel mechano-acoustic technique and instrument for diagnosis of cartilage degeneration. *Physiol Meas*, 23:491–503, 2002.

88. Laasanen M. S., Töyräs J., Korhonen R. K., Rieppo J., Saarakkala S., Nieminen M. T., Hirvonen J. and Jurvelin J. S. Biomechanical properties of knee articular cartilage. *Biorheology*, 40:133–40, 2003.

89. Lai W. M., Hou J. S. and Mow V. C. A triphasic theory for the swelling and deformation behaviors of articular cartilage. *J Biomech Eng*, 113(3):245–58, 1991.

90. Lai W. M. and Mow V. C. Drag-induced compression of articular cartilage during a permeation experiment. *Biorheology*, 17(1-2):111–23, 1980.

91. Lai W. M., Mow V. C. and Roth V. Effects of nonlinear strain-dependent permeability and rate of compression on the stress behavior of articular cartilage. *J Biomech Eng*, 103(2):61–6, 1981.

92. Li L., Buschmann M. D. and Shirazi-Adl A. The role of fibril reinforcement in the mechanical behavior of cartilage. *Biorheology*, 39(1-2):89–96, 2002.

93. Li L. P., Buschmann M. D. and Shirazi-Adl A. A fibril reinforced nonhomogeneous poroelastic model for articular cartilage: inhomogeneous response in unconfined compression. *J Biomech*, 33(12):1533–41, 2000.

94. Li L. P., Buschmann M. D. and Shirazi-Adl A. Strain-rate dependent stiffness of articular cartilage in unconfined compression. *J Biomech Eng*, 125(2):161–8, 2003.

95. Li L. P. and Herzog W. Strain-rate dependence of cartilage stiffness in unconfined compression: the role of fibril reinforcement versus tissue volume change in fluid pressurization. *J Biomech*, 37(3):375–82, 2004.

96. Li L. P., Herzog W., Korhonen R. K. and Jurvelin J. S. The role of viscoelasticity of collagen fibers in articular cartilage: axial tension versus compression. *Med Eng Phys*, 27(1):47–53, 2005.

97. Li L. P., Korhonen R. K., Iivarinen J., Jurvelin J. S. and Herzog W. Fluid pressure driven fibril reinforcement in creep and relaxation tests of articular cartilage. *Med Eng Phys*, 30(2):182–9, 2008.

98. Li L. P., Soulhat J., Buschmann M. D. and Shirazi-Adl A. Nonlinear analysis of cartilage in unconfined ramp compression using a fibril reinforced poroelastic model. *Clin Biomech (Bristol, Avon)*, 14(9):673–82, 1999.

99. Linn F. C. and Sokoloff L. Movement and composition of interstitial fluid of cartilage. *Arthritis Rheum*, 8(4):481–94, 1965.

100. Lipshitz H., Etheredge R. d. and Glimcher M. J. In vitro wear of articular cartilage. *J Bone Joint Surg Am*, 57(4):527–34, 1975.

101. Lu X. L., Miller C., Chen F. H., Guo X. E. and Mow V. C. The generalized triphasic correspondence principle for simultaneous determination of the mechanical properties and proteoglycan content of articular cartilage by indentation. *J Biomech*, 40(11):2434–41, 2007.

102. Lu X. L., Sun D. D., Guo X. E., Chen F. H., Lai W. M. and Mow V. C. Indentation determined mechanoelectrochemical properties and fixed charge density of articular cartilage. *Ann Biomed Eng*, 32(3):370–9, 2004.

103. Lyyra T., Arokoski J. P., Oksala N., Vihko A., Hyttinen M., Jurvelin J. S. and Kiviranta I. Experimental validation of arthroscopic cartilage stiffness measurement using enzymatically degraded cartilage samples. *Phys Med Biol*, 44(2):525–35, 1999.

104. Lyyra T., Kiviranta I., Vaatainen U., Helminen H. J. and Jurvelin J. S. In vivo characterization of indentation stiffness of articular cartilage in the normal human knee. *J Biomed Mater Res*, 48(4):482–7, 1999.

105. Mak A. F. The apparent viscoelastic behavior of articular cartilage-the contributions from the intrinsic matrix viscoelasticity and interstitial fluid flows. *Transactions of the ASME. J Biomech Eng*, 108(2):123–30, 1986.

106. Mak A. F., Lai W. M. and Mow V. C. Biphasic indentation of articular cartilage. I. Theoretical analysis. *J Biomech*, 20(7):703–14, 1987.

107. Mankin H. J., Dorfman H., Lippiello L. and Zarins A. Biochemical and metabolic abnormalities in articular cartilage from osteo-arthritic human hips. II. Correlation of morphology with biochemical and metabolic data. *J Bone Joint Surg Am*, 53(3):523–37, 1971.

108. Mankin H. J. and Thrasher A. Z. Water content and binding in normal and osteoarthritic human cartilage. *J Bone Joint Surg Am*, 57(1):76–80, 1975.

109. Mansour J. M. and Mow V. C. The permeability of articular cartilage under compressive strain and at high pressures. *J Bone Joint Surg Am*, 58(4):509–16, 1976.

110. Maroudas A. Physicochemical properties of cartilage in the light of ion exchange theory. *Biophys J*, 8(5):575–95, 1968.

111. Maroudas A. Biophysical chemistry of cartilaginous tissues with special reference to solute and fluid transport. *Biorheology*, 12(3-4):233–48, 1975.

112. Maroudas A. and Bannon C. Measurement of swelling pressure in cartilage and comparison with the osmotic pressure of constituent proteoglycans. *Biorheology*, 18(3-6):619–32, 1981.

113. Maroudas A. and Bullough P. Permeability of articular cartilage. *Nature*, 219(160):1260–1, 1968.

114. Maroudas A., Wachtel E., Grushko G., Katz E. P. and Weinberg P. The effect of osmotic and mechanical pressures on water partitioning in articular cartilage. *Biochim Biophys Acta*, 1073(2):285–94, 1991.

115. Maroudas A. I. Balance between swelling pressure and collagen tension in normal and degenerate cartilage. *Nature*, 260(5554):808–9, 1976.

116. Meachim G., Denham D., Emery I. H. and Wilkinson P. H. Collagen alignments and artificial splits at the surface of human articular cartilage. *J Anat*, 118(1):101–18, 1974.

117. Mow V. C., Fithian D. C. and Kelly M. A. Fundamentals of articular cartilage and meniscus biomechanics. In Ewing J. W., editor, *Articular cartilage and knee joint function: basic science and arthroscopy*, pages 1–18. Raven Press Ltd., New York, 1990.

118. Mow V. C., Kuei S. C., Lai W. M. and Armstrong C. G. Biphasic creep and stress relaxation of articular cartilage in compression: Theory and experiments. *J Biomech Eng*, 102(1):73–84, 1980.

119. Mow V. C., Ratcliffe A. and Poole A. R. Cartilage and diarthrodial joints as paradigms for hierarchical materials and structures. *Biomaterials*, 13(2):67–97, 1992.

120. Mow V. C., Zhu W. and Ratcliffe A. Structure and function of articular cartilage and meniscus. In Mow V. C. and Hayes W. C., editors, *Basic orthopaedic biomechanics*, pages 143–198. Raven Press, Ltd, New York, 1991.

121. Muir H. Proteoglycans as organizers of the intercellular matrix. *Biochem Soc Trans*, 11(6):613–22, 1983.

122. Nieminen H. J., Julkunen P., Töyräs J. and Jurvelin J. S. Ultrasound Speed in Articular Cartilage under Mechanical Compression. *Ultrasound Med Biol*, 30(11):1755–66, 2007.

123. Nieminen H. J., Saarakkala S., Laasanen M. S., Hirvonen J., Jurvelin J. S. and Töyräs J. Ultrasound attenuation in normal and spontaneously degenerated articular cartilage. *Ultrasound Med Biol*, 30:493–500, 2004.

124. Nieminen M. T., Töyräs J., Laasanen M., Silvennoinen J., Helminen H. J. and Jurvelin J. S. Prediction of biomechanical properties of articular cartilage with quantitative magnetic resonance imaging. *J Biomech*, 37:321–8, 2004.

125. Nieminen M., Töyräs J., Rieppo J., Silvennoinen M., Hakumäki J., Hyttinen M., Helminen H. and Jurvelin J. T2 relaxation reveals spatial collagen architecture in articular cartilage: a comparative quantitative MRI and polarized light microscopic study. *Magn Reson Med*, 46:487–93, 2001.

126. Nissi M., Rieppo J., Töyräs J., Laasanen M., Kiviranta I., Jurvelin J. S. and Nieminen M. T. MRI quantitation of proteoglycans with dGEMRIC in human, bovine and porcine articular cartilage. In *Trans Orthop Res Soc*, volume 29, page 1004, 2004.

127. Nissi M. J., Rieppo J., Töyräs J., Laasanen M. S., Kiviranta I., Jurvelin J. S. and Nieminen M. T. T(2) relaxation time mapping reveals age- and species-related diversity of collagen network architecture in articular cartilage. *Osteoarthritis Cartilage*, 14(12):1265–71, 2006.

128. Nissi M. J., Rieppo J., Töyräs J., Laasanen M. S., Kiviranta I., Nieminen M. T. and Jurvelin J. S. Estimation of mechanical properties of articular cartilage with MRI - dGEMRIC, T2 and T1 imaging in different species with variable stages of maturation. *Osteoarthritis Cartilage*, 15(10):1141–8, 2007.

129. Palmoski M., Perricone E. and Brandt K. D. Development and reversal of a proteoglycan aggregation defect in normal canine knee cartilage after immobilization. *Arthritis Rheum*, 22(5):508–17, 1979.

130. Panula H. E., Hyttinen M. M., Arokoski J. P., Långsjö T. K., Pelttari A., Kiviranta I. and Helminen H. J. Articular cartilage superficial zone collagen birefringence reduced and cartilage thickness increased before surface fibrillation in experimental osteoarthritis. *Ann Rheum Dis*, 57(4):237–45, 1998.

131. Park S., Krishnan R., Nicoll S. B. and Ateshian G. A. Cartilage interstitial fluid load support in unconfined compression. *J Biomech*, 36(12):1785–96, 2003.

132. Parsons J. R. and Black J. Mechanical behavior of articular cartilage quantitative changes with enzymatic alteration of the proteoglycan fraction. *Bull Hosp Jt Dis Orthop Inst*, 47(1):13–30, 1987.

133. Pins G. D., Huang E. K., Christiansen D. L. and Silver F. H. Effects of Static Axial Strain on the Tensile Properties and Failure Mechanisms of Self-Assembled Collagen Fibers. *J Appl Polym Sci*, 63(11):1429–40, 1997.

134. Potter K., Kidder L. H., Levin I. W., Lewis E. N. and Spencer R. G. Imaging of collagen and proteoglycan in cartilage sections using Fourier transform infrared spectral imaging. *Arthritis Rheum*, 44(4):846–55, 2001.

135. Qu C. J., Rieppo J., Hyttinen M. M., Lammi M. J., Kiviranta I., Kurkijärvi J., Jurvelin J. S. and Töyräs J. Human articular cartilage proteoglycans are not undersulfated in osteoarthritis. *Connect Tissue Res*, 48(1):27–33, 2007.

136. Quinn T. M., Dierickx P. and Grodzinsky A. J. Glycosaminoglycan network geometry may contribute to anisotropic hydraulic permeability in cartilage under compression. *J Biomech*, 34(11):1483–90, 2001.

137. Quinn T. M. and Morel V. Microstructural modeling of collagen network mechanics and interactions with the proteoglycan gel in articular cartilage. *Biomech Model Mechanobiol*, 6(1-2):73–82, 2007.

138. Radin E. L. and Rose R. M. Role of subchondral bone in the initiation and progression of cartilage damage. *Clin Orthop Relat Res*, (213):34–40, 1986.

139. Ratcliffe A., Fryer P. R. and Hardingham T. E. The distribution of aggregating proteoglycans in articular cartilage: comparison of quantitative immunoelectron microscopy with radioimmunoassay and biochemical analysis. *J Histochem Cytochem*, 32(2):193–201, 1984.

140. Reibetanz U. and Gründer W. Age-development of Articular Cartilage Structures of Sheep. In *Proc. Intl. Soc. Mag. Reson. Med.*, volume 11, page 1502, 2003.

141. Rieppo J., Hallikainen J., Jurvelin J. S., Helminen H. J. and Hyttinen M. M. Novel quantitative polarization microscopic assessment of articular cartilage and bone collagen birefringence, orientation and anisotropy. In *Trans Orthop Res Soc*, volume 28, page 570, 2003.

142. Rieppo J., Hallikainen J., Jurvelin J. S., Kiviranta I., Helminen H. J. and Hyttinen M. M. Practical considerations in the use of polarized light microscopy in the analysis of the collagen network in articular cartilage. *Microsc Res Tech*, 71(4):279–87, 2008.

143. Rieppo J., Heinz R., Töyräs J., Laasanen M. S., Saarakkala S., Jurvelin J. S., Hyttinen M. M. and Helminen H. J. FTIR imaging discerns different stages of cartilage degeneration. In *Trans Orthop Res Soc*, volume 28, 2003.

144. Rieppo J., Hyttinen M. M., Halmesmäki E., Ruotsalainen H., Vasara A., Kiviranta I., Jurvelin J. S. and Helminen H. J. Remodelation of collagen network architecture during cartilage maturation. In *Trans Orthop Res Soc*, volume 29, page 549, 2004.

145. Rieppo J., Hyttinen M. M., Laasanen M., Nieminen M. T., Långsjö T. K., Vasara A., Kiviranta I., Jurvelin J. S. and Helminen H. J. Quantitative characterization of articular cartilage repair tissue. In *Trans Orthop Res Soc*, volume 29, page 661, 2004.

146. Rieppo J., Hyttinen M. M., Lappalainen R., Jurvelin J. S. and Helminen H. J. Spatial determination of water, collagen and proteoglycan contents by Fourier Transform Infrared imaging and digital densitometry. In *Trans Orthop Res Soc*, volume 29, page 1021, 2004.

147. Rieppo J., Julkunen P., Jurvelin J. S. and Helminen H. J. Compositional changes of articular cartilage under static loading conditions: Quantitative analysis with FT-IRIS and FE model. In *Trans Orthop Res Soc*, volume 32, page 626, 2007.

148. Rieppo J., Ruotsalainen H., Töyräs J., Kurkijärvi J., Kiviranta I., Helminen H. J. and Jurvelin J. S. FT-IRIS derived collagen and proteoglycan parameters predict biomechanical properties of human articular cartilage. In *Trans Orthop Res Soc*, volume 30, page 51, 2005.

149. Rieppo J., Toyras J., Nieminen M. T., Kovanen V., Hyttinen M. M., Korhonen R. K., Jurvelin J. S. and Helminen H. J. Structure-function relationships in enzymatically modified articular cartilage. *Cells Tissues Organs*, 175(3):121–32, 2003.

150. Rivers P. A., Rosenwasser M. P., Mow V. C., Pawluk R. J., Strauch R. J., Sugalski M. T. and Ateshian G. A. Osteoarthritic changes in the biochemical composition of thumb carpometacarpal joint cartilage and correlation with biomechanical properties. *J Hand Surg [Am]*, 25:889–98, 2000.

151. Rodriguez R. R., Seegmiller R. E., Stark M. R. and Bridgewater L. C. A type XI collagen mutation leads to increased degradation of type II collagen in articular cartilage. *Osteoarthritis Cartilage*, 12(4):314–20, 2004.

152. Roos H., Lauren M., Adalberth T., Roos E. M., Jonsson K. and Lohmander L. S. Knee osteoarthritis after meniscectomy: prevalence of radiographic changes after twenty-one years, compared with matched controls. *Arthritis Rheum*, 41(4):687–93, 1998.

153. Roth V. and Mow V. C. The intrinsic tensile behavior of the matrix of bovine articular cartilage and its variation with age. *J Bone Joint Surg Am*, 62(7):1102–17, 1980.

154. Rubenstein J. D., Kim J. K., Morova-Protzner I., Stanchev P. L. and Henkelman R. M. Effects of collagen orientation on MR imaging characteristics of bovine articular cartilage. *Radiology*, 188(1):219–26, 1993.

155. Saarakkala S., Korhonen R. K., Laasanen M., Töyräs J., Rieppo J. and Jurvelin J. S. Mechano-acoustic determination of Young's modulus of articular cartilage. *Biorheology*, 41:167–79, 2004.

156. Saarakkala S., Laasanen M. S., Jurvelin J. S., Törrönen K., Lammi M. J., Lappalainen R. and Töyräs J. Ultrasound indentation of normal and spontaneously degenerated bovine articular cartilage. *Osteoarthritis Cartilage*, 11:697–705, 2003.

157. Sah R. L., Yang A. S., Chen A. C., Hant J. J., Halili R. B., Yoshioka M., Amiel D. and Coutts R. D. Physical properties of rabbit articular cartilage after transection of the anterior cruciate ligament. *J Orthop Res*, 15(2):197–203, 1997.

158. Schwartz D. E., Choi Y., Sandell L. J. and Hanson W. R. Quantitative analysis of collagen, protein and DNA in fixed, paraffin-embedded and sectioned tissue. *Histochem J*, 17(6):655–63, 1985.

159. Seog J., Dean D., Rolauffs B., Wu T., Genzer J., Plaas A. H., Grodzinsky A. J. and Ortiz C. Nanomechanics of opposing glycosaminoglycan macromolecules. *J Biomech*, 38(9):1789–97, 2005.

160. Setton L. A., Mow V. C. and Howell D. S. Mechanical behavior of articular cartilage in shear is altered by transection of the anterior cruciate ligament. *J Orthop Res*, 13(4):473–82, 1995.

161. Setton L. A., Mow V. C., Muller F. J., Pita J. C. and Howell D. S. Mechanical properties of canine articular cartilage are significantly altered following transection of the anterior cruciate ligament. *J Orthop Res*, 12(4):451–63, 1994.

162. Setton L. A., Zhu W. and Mow V. C. The biphasic poroviscoelastic behavior of articular cartilage: role of the surface zone in governing the compressive behavior. *J Biomech*, 26(4-5):581–92, 1993.

163. Shapiro E. M., Borthakur A., Kaufman J. H., Leigh J. S. and Reddy R. Water distribution patterns inside bovine articular cartilage as visualized by 1H magnetic resonance imaging. *Osteoarthritis Cartilage*, 9(6):533–8, 2001.

164. Shapiro F. and Glimcher M. J. Induction of osteoarthrosis in the rabbit knee joint. *Clin Orthop Relat Res*, (147):287–95, 1980.

165. Shirazi R. and Shirazi-Adl A. Deep vertical collagen fibrils play a significant role in mechanics of articular cartilage. *J Orthop Res*, 26(5):608–15, 2008.

166. Soltz M. A. and Ateshian G. A. Experimental verification and theoretical prediction of cartilage interstitial fluid pressurization at an impermeable contact interface in confined compression. *J Biomech*, 31(10):927–34, 1998.

167. Soltz M. A. and Ateshian G. A. A Conewise Linear Elasticity mixture model for the analysis of tension- compression nonlinearity in articular cartilage. *J Biomech Eng*, 122(6):576–86, 2000.

168. Soulhat J., Buschmann M. D. and Shirazi-Adl A. A fibril-network-reinforced biphasic model of cartilage in unconfined compression. *J Biomech Eng*, 121(3):340–7, 1999.

169. Speer D. P. and Dahners L. The collagenous architecture of articular cartilage. Correlation of scanning electron microscopy and polarized light microscopy observations. *Clin Orthop Relat Res*, (139):267–75, 1979.

170. Spilker R. L., Suh J. K. and Mow V. C. A finite element analysis of the indentation stress-relaxation response of linear biphasic articular cartilage. *J Biomech Eng*, 114(2):191–201, 1992.

171. Suh J. K. and Bai S. Finite element formulation of biphasic poroviscoelastic model for articular cartilage. *J Biomech Eng*, 120(2):195–201, 1998.

172. Sun D. D., Guo X. E., Likhitpanichkul M., Lai W. M. and Mow V. C. The influence of the fixed negative charges on mechanical and electrical behaviors of articular cartilage under unconfined compression. *J Biomech Eng*, 126(1):6–16, 2004.

173. Thambyah A. and Broom N. Micro-anatomical response of cartilage-on-bone to compression: mechanisms of deformation within and beyond the directly loaded matrix. *J Anat*, 209(5):611–22, 2006.

174. Thambyah A. and Broom N. On how degeneration influences load-bearing in the cartilage-bone system: a microstructural and micromechanical study. *Osteoarthritis Cartilage*, 15(12):1410–23, 2007.

175. Torzilli P. A. Influence of cartilage conformation on its equilibrium water partition. *J Orthop Res*, 3(4):473–83, 1985.

176. Trickey W. R., Vail T. P. and Guilak F. The role of the cytoskeleton in the viscoelastic properties of human articular chondrocytes. *J Orthop Res*, 22(1):131–9, 2004.

177. Töyräs J., Laasanen M. S., Saarakkala S., Lammi M. J., Rieppo J., Kurkijarvi J., Lappalainen R. and Jurvelin J. S. Speed of sound in normal and degenerated bovine articular cartilage. *Ultrasound Med Biol*, 29(3):447–54, 2003.

178. Töyräs J., Rieppo J., Nieminen M. T., Helminen H. J. and Jurvelin J. S. Characterization of enzymatically induced degradation of articular cartilage using high frequency ultrasound. *Phys Med Biol*, 44(11):2723–33, 1999.

179. Urban J. P. and McMullin J. F. Swelling pressure of the lumbar intervertebral discs: influence of age, spinal level, composition, and degeneration. *Spine*, 13(2):179–87, 1988.

180. van der Kraan P. M., de Lange J., Vitters E. L., van Beuningen H. M., van Osch G. J., van Lent P. L. and van den Berg W. B. Analysis of changes in proteoglycan content in murine articular cartilage using image analysis. *Osteoarthritis Cartilage*, 2(3):207–14, 1994.

181. van der Voet A. A comparison of finite element codes for the solution of biphasic poroelastic problems. *Proc Inst Mech Eng [H]*, 211(2):209–11, 1997.

182. Venn M. and Maroudas A. Chemical composition and swelling of normal and osteoarthrotic femoral head cartilage. I. Chemical composition. *Ann Rheum Dis*, 36(2):121–9, 1977.

183. Verzijl N., DeGroot J., Ben Z. C., Brau-Benjamin O., Maroudas A., Bank R. A., Mizrahi J., Schalkwijk C. G., Thorpe S. R., Baynes J. W., Bijlsma J. W., Lafeber F. P. and TeKoppele J. M. Crosslinking by advanced glycation end products increases the stiffness of the collagen network in human articular cartilage: a possible mechanism through which age is a risk factor for osteoarthritis. *Arthritis Rheum*, 46(1):114–23, 2002.

184. Wayne J. S., Kraft K. A., Shields K. J., Yin C., Owen J. R. and Disler D. G. MR imaging of normal and matrix-depleted cartilage: correlation with biomechanical function and biochemical composition. *Radiology*, 228(2):493–9, 2003.

185. Weiss J. A. and Maakestad B. J. Permeability of human medial collateral ligament in compression transverse to the collagen fiber direction. *J Biomech*, 39(2):276–83, 2006.

186. Wheaton A. J., Dodge G. R., Borthakur A., Kneeland J. B., Schumacher H. R. and Reddy R. Detection of changes in articular cartilage proteoglycan by T1p magnetic resonance imaging. *J Orthop Res*, 23:102–8, 2005.

187. Wilson W., Driessen N. J., van Donkelaar C. C. and Ito K. Prediction of collagen orientation in articular cartilage by a collagen remodeling algorithm. *Osteoarthritis Cartilage*, 14(11):1196–1202, 2006.

188. Wilson W., Huyghe J. M. and van Donkelaar C. C. A composition-based cartilage model for the assessment of compositional changes during cartilage damage and adaptation. *Osteoarthritis Cartilage*, 14(6):554–60, 2006.

189. Wilson W., Huyghe J. M. and van Donkelaar C. C. Depth-dependent compressive equilibrium properties of articular cartilage. *Biomech Model Mechanobiol*, 6(1-2):43–53, 2007.

190. Wilson W., van Donkelaar C. C., van Rietbergen B. and Huiskes R. A fibril-reinforced poroviscoelastic swelling model for articular cartilage. *J Biomech*, 38(6):1195–204, 2005.

191. Wilson W., van Donkelaar C. C., van Rietbergen B., Ito K. and Huiskes R. Stresses in the local collagen network of articular cartilage: a poroviscoelastic fibril-reinforced element study. *J Biomech*, 37:357–66, 2004.

192. Wilson W., van Donkelaar C. C., Van Rietbergen B., Ito K. and Huiskes R. Erratum to 'Stresses in the local collagen network of articular cartilage: a poroviscoelastic fibril-reinforced finite element study' [Journal of Biomechanics 37 (2004) 357-366] and 'A fibril-reinforced poroviscoelastic swelling model for articular cartilage' [Journal of Biomechanics 38 (2005) 1195-1204]. *J Biomech*, 38:2138–40, 2005.

193. Wu J. J., Woods P. E. and Eyre D. R. Identification of cross-linking sites in bovine cartilage type IX collagen reveals an antiparallel type II-type IX molecular relationship and type IX to type IX bonding. *J Biol Chem*, 267(32):23007–14, 1992.

194. Wu J. Z. and Herzog W. Elastic anisotropy of articular cartilage is associated with the microstructures of collagen fibers and chondrocytes. *J Biomech*, 35(7):931–42, 2002.

195. Wu J. Z. and Herzog W. Simulating the swelling and deformation behaviour in soft tissues using a convective thermal analogy. *Biomed Eng Online*, 1:8, 2002.

196. Xia Y. Heterogeneity of cartilage laminae in MR imaging. *J Magn Reson Imaging*, 11(6):686–93, 2000.

197. Xia Y., Moody J. B. and Alhadlaq H. Orientational dependence of T2 relaxation in articular cartilage: A microscopic MRI (microMRI) study. *Magn Reson Med*, 48(3):460–9, 2002.

198. Xia Y., Moody J. B., Alhadlaq H. and Hu J. Imaging the physical and morphological properties of a multi-zone young articular cartilage at microscopic resolution. *J Magn Reson Imaging*, 17(3):365–74, 2003.

199. Xia Y., Moody J. B., Burton-Wurster N. and Lust G. Quantitative in situ correlation between microscopic MRI and polarized light microscopy studies of articular cartilage. *Osteoarthritis Cartilage*, 9(5):393–406, 2001.

200. Xia Y., Ramakrishnan N. and Bidthanapally A. The depth-dependent anisotropy of articular cartilage by Fourier transform infrared imaging. *Osteoarthritis Cartilage*, 15(7):780–8, 2007.

201. Young R. D., Lawrence P. A., Duance V. C., Aigner T. and Monaghan P. Immunolocalization of type III collagen in human articular cartilage prepared by high-pressure cryofixation, freeze-substitution, and low- temperature embedding. *J Histochem Cytochem*, 43(4):421–7, 1995.

ORIGINAL PUBLICATIONS

## Kuopio University Publications C. Natural and Environmental Sciences

**C 213. Georgiadis, Stefanos.** State-Space Modeling and Bayesian Methods for Evoked Potential Estimation.
2007. 179 p. Acad. Diss.

**C 214. Sierpowska, Joanna.** Electrical and dielectric characterization of trabecular bone quality.
2007. 92 p. Acad. Diss.

**C 215. Koivunen, Jari.** Effects of conventional treatment, tertiary treatment and disinfection processes on hygienic and physico-chemical quality of municipal wastewaters.
2007. 80 p. Acad. Diss.

**C 216. Lammentausta, Eveliina.** Structural and mechanical characterization of articular cartilage and trabecular bone with quantitative NMR .
2007. 89 p. Acad. Diss.

**C 217. Veijalainen, Anna-Maria.** Sustainable organic waste management in tree-seedling production.
2007. 114 p. Acad. Diss.

**C 218. Madetoja, Elina.** Novel process line approach for model-based optimization in papermaking.
2007. 125 p. Acad. Diss.

**C 219. Hyttinen, Marko.** Formation of organic compounds and subsequent emissions from ventilation filters.
2007. 80 p. Acad. Diss.

**C 220. Plumed-Ferrer, Carmen.** Lactobacillus plantarum: from application to protein expression.
2007. 60 p. Acad. Diss.

**C 221. Saavalainen, Katri.** Evaluation of the mechanisms of gene regulation on the chromatin level at the example of human hyaluronan synthase 2 and cyclin C genes.
2007. 102 p. Acad. Diss.

**C 222. Koponen, Hannu T.** Production of nitrous oxide ($N_2O$) and nitric oxide (NO) in boreal agricultural soils at low temperature.
2007. 102 p. Acad. Diss.

**C 223. Korkea-aho, Tiina.** Epidermal papillomatosis in roach (Rutilus rutilus) as an indicator of environmental stressors.
2007. 53 p. Acad. Diss.

**C 224. Räisänen, Jouni.** Fourier transform infrared (FTIR) spectroscopy for monitoring of solvent emission rates from industrial processes.
2007. 75 p. Acad. Diss.

**C 225. Nissinen, Anne.** Towards ecological control of carrot psyllid (Trioza apicalis).
2008. 128 p. Acad. Diss.

**C 226. Huttunen, Janne.** Approximation and modellingerrors in nonstationary inverse problems.
2008. 56 p. Acad. Diss.

**C 227. Freiwald, Vera.** Does elevated ozone predispose northern deciduous tree species to abiotic and biotic stresses?
2008. 109 p. Acad. Diss.